

## Cosmological Results from Five Years of 30 GHz CMB Intensity Measurements with the Cosmic Background Imager

J.L. Sievers<sup>1</sup>, B.S. Mason<sup>2</sup>, L. Weintraub<sup>3</sup>, C. Achermann<sup>4</sup>, P. Altamirano<sup>4</sup>, J.R. Bond<sup>1</sup>, L. Bronfman<sup>4</sup>, R. Bustos<sup>13</sup>, C. Contaldi<sup>7</sup>, C. Dickinson<sup>3,8</sup>, M.E. Jones<sup>9</sup>, J. May<sup>4</sup>, S.T. Myers<sup>11</sup>, N. Oyarce<sup>4</sup>, S. Padin<sup>6</sup>, T.J. Pearson<sup>3</sup>, M. Pospieszalski<sup>12</sup>, A.C.S. Readhead<sup>3</sup>, R. Reeves<sup>13</sup>, M. C. Shepherd<sup>3</sup>, A. C. Taylor<sup>9</sup>, S. Torres<sup>13</sup>

### ABSTRACT

We present final results on the angular power spectrum of total intensity anisotropies in the Microwave Background from the Cosmic Background Imager (CBI). Our analysis includes all primordial anisotropy data collected between January 2000 and April 2005, and benefits significantly from an improved maximum likelihood analysis pipeline. It also includes results from a 30 GHz foreground survey conducted with the Green Bank Telescope (GBT) which places significant constraints on the possible contamination due to foreground point

---

<sup>1</sup>Canadian Institute for Theoretical Astrophysics, University of Toronto, ON M5S 3H8, Canada

<sup>2</sup>National Radio Astronomy Observatory, 520 Edgemont Road, Charlottesville, VA 22903

<sup>3</sup>Owens Valley Radio Observatory, California Institute of Technology, Pasadena, CA

<sup>4</sup>Departamento de Astronomía, Universidad de Chile, Santiago, Chile

<sup>6</sup>Kavli Institute for Cosmological Physics, Department of Astronomy and Astrophysics, University of Chicago, Chicago, IL 60637

<sup>7</sup>Department of Physics, Imperial College, London, UK

<sup>8</sup>Infrared Processing & Analysis Center, California Institute of Technology, M/S 220-6, 1200 E. California Blvd., Pasadena, CA 91125

<sup>9</sup>Astrophysics, Oxford University, Keble Road, Oxford OX1 3RH, UK

<sup>10</sup>U.C. Berkeley Astronomy

<sup>11</sup>National Radio Astronomy Observatory, Socorro, NM 87801

<sup>12</sup>NRAO New Technology Center, Charlottesville VA 22903

<sup>13</sup>Departamento de Ingeniería Eléctrica, Universidad de Concepción, Concepción, Chile

sources. We improve on previous CBI results by about a factor of two in the damping tail. These data confirm, at  $\sim 3\sigma$ , the existence of an excess of power over intrinsic CMB anisotropy on small angular scales ( $\ell > 1800$ ). Using the GBT survey, we find currently known radio source populations are not capable of generating the power; a new population of faint sources with steeply rising spectral indices would be required to explain the excess with sources. Extensive testing does not reveal any instrumental effect capable of giving rise to the observed excess. We also present a full cosmological parameter analysis of the new CBI power spectrum, the WMAP 5-year data, and the latest ACBAR data, self-consistently including in the analysis the foreground signal from the Sunyaev-Zel'dovich Effect (SZE) from galaxy clusters. With CBI alone, the full parameter analysis finds the excess is  $1.6\sigma$  above the level expected for a  $\sigma_8 = 0.8$  universe. We fit two different SZ templates to the power spectrum and find they give markedly different inferred  $\sigma_8$  values suggesting more theoretical work is required. We find the addition of high- $\ell$  CMB data substantially improves constraints on cosmic string contributions to the TT power spectrum as well as the running of the scalar spectral index  $n_{run}$ , but that  $n_{run}$  is quite sensitive to the level of the SZE. We also present forecasts for what other experiments should see at different frequencies and angular resolutions given the excess power observed by CBI. We find that the reported high  $\ell$  bandpowers from current high resolution CMB bolometer experiments are consistent with each other and CBI if the excess power is due to the SZE at the CBI-level of  $2.5 \pm 1$  times the  $\sigma_8 = 0.8$  standard SZ template. This is not the case if the CBI excess source has a flat frequency dependence in thermodynamic temperature.

*Subject headings:* cosmology, cosmic microwave background

## 1. Introduction

Measurements of Cosmic Microwave Background (CMB) anisotropies in total intensity (de Bernardis et al. 2000; Hanany et al. 2000; Halverson et al. 2002; Pearson et al. 2003; Dickinson et al. 2004; Nolta et al. 2008) and polarization (Kovac et al. 2002; Readhead et al. 2004b; Sievers et al. 2007; Montroy et al. 2006; Ade et al. 2008; Pryke et al. 2008; Nolta et al. 2008) over the past decade— together with a range of other cosmological measurements (Riess et al. 1998; Perlmutter et al. 1999; Freedman et al. 2001)— have provided striking

confirmation of the inflationary structure formation paradigm. Key elements of this picture which have been confirmed are: that the universe is spatially flat; that anisotropies in the microwave background formed via simple causal processes from an approximately scale-invariant spectrum of (probably adiabatic) primordial inhomogeneities; and that the gravitational instability picture of subsequent structure formation from the collapse of baryons and dark matter in an expanding metric. In spite of what must, on the whole, be described as stunning experimental confirmation of the inflationary predictions, several surprises emerged, and tensions and ambiguities in our understanding of the data remain. Chief amongst these are the necessity for a (presently dynamically dominant) dark energy component, some anomalies in the large-angle WMAP data, and a  $\sim 3\sigma$  excess of power on small angular scales (Mason et al. 2003; Readhead et al. 2004a; Kuo et al. 2004; Dawson et al. 2006; Kuo et al. 2007; Reichardt et al. 2008). A number of secondary anisotropies— predominantly the Sunyaev-Zel’dovich Effect (SZE) from galaxy clusters— are expected to contribute on small angular scales, thus providing a view of the more recent evolution of large-scale structure through the CMB.

The Cosmic Background Imager (CBI) is a 30 GHz interferometer that measures CMB anisotropies from  $\ell \sim 400$  to  $\ell \sim 3000$ . The instrument has been described in detail in Padin et al. (2002). From January 2000 through November of 2001 the CBI surveyed  $\sim 98\text{deg}^2$  of sky. Results from this work were presented in Padin et al. (2001) (hereafter Paper 1), Mason et al. (2003) (Paper 2), Pearson et al. (2003) (Paper 3), and Readhead et al. (2004a) (Paper 7). Following this campaign the instrument was upgraded to focus primarily on CMB polarization observations, which were conducted from September 2002 through April 2005. The fields observed in the polarization campaign encompassed  $\sim 115\text{deg}^2$  in all, and partially overlapped with the fields observed in the total-intensity campaign. The total area covered in the combined datasets is  $143\text{deg}^2$ . While roughly half of the CBI baselines were cross-polarized for these observations (appropriate to measure polarization), the other half were co-polar and thus improve results on the TT power spectrum. Results from the polarization campaign are presented in Readhead et al. (2004b) (Paper 8) and Sievers et al. (2007) (Paper 9). In this paper we combine all of these data to present the final TT power spectrum from five years of CBI measurements. We also examine the implications of the observed high- $\ell$  signal in the context of a full cosmological parameter analysis including a treatment of uncertainties in the SZ foreground models.

A key limiting factor in interpreting the high- $\ell$  excess measured by CBI has been uncertainties associated with the extragalactic point source correction. Extragalactic sources reduced the sensitivity of the CBI at high- $\ell$  in two ways: by requiring a substantial amount of data to be “thrown out” owing to possible contamination from known sources, and through the uncertainty in the power spectrum of fainter sources extrapolated from number counts.

In order to address the second issue, we conducted a 30 GHz survey with the GBT and the OVRO 40-m telescope, covering a total of 3562 NVSS (Condon et al. 1998) sources in the CBI fields; this survey is described in the companion paper Mason et al. (2008). This survey has allowed us to place much tighter constraints on the point source foreground contribution to our power spectrum, which we have quantified and included in this analysis. Because of the potential of source variability, we do not attempt to reclaim the sky area under NVSS sources that are not detected by the GBT.

The structure of the paper is as follows. In § 2 we briefly summarize the data. § 3 provides a description of improvements to our analysis algorithms, describes tests performed on the data, and summarizes our knowledge of foregrounds (chiefly discrete sources) in the CBI fields. In § 4 we present the CBI power spectrum, discuss the significance and characteristics of the high- $\ell$  excess signal, and give constraints on cosmological parameters from this. § 5 summarizes our findings. We describe our spectrum-fitting procedure in Appendix A.

## 2. Observations

For this analysis we use data collected on both the CBI total intensity fields from Readhead et al. (2004a) and the intensity data from the CBI polarization fields described in Sievers et al. (2007). The fields, observing strategies, data reduction, and calibration are described in detail in Papers 2, 3, 7, 8, and 9; here we simply summarize the contents of these papers.

The CBI total intensity and polarization fields were spaced by  $\approx 6$  hours in Right Ascension (centered near 02h, 08h, 14h, and 20h) and are near the celestial equator. The polarization and total intensity fields overlap but are not identical. To test for systematics and obtain higher signal-to-noise ratio at high- $\ell$ , some very deep integrations on individual pointings were performed in each campaign. During the total intensity campaign, all integration time at 8h was concentrated in a single pointing; the 14h and 20h mosaic fields also contained one pointing each on which significantly more integration time was acquired. During the polarization campaign, observations at 20h concentrated on a single  $1\times 6$  strip instead of  $6\times 6$  mosaics. These fields are summarized in Table 1. The deep 14h and 20h fields, while within the total intensity mosaics of these regions and collected and analyzed identically, are listed separately in this table since for some tests we analyze only the deep data.

The largest source of systematic errors in the CBI data is a ground spillover signal, which

is strongest on the short baselines. We find this signal is stable over timescales of at least 20 minutes. For the total intensity observations, contaminating ground signal was removed by differencing pairs of individual pointings separated by 8 minutes in Right Ascension. For the polarization mosaics 6 successive pointings were observed in succession and a single common mode removed from matched visibilities.

All data are calibrated with respect to the 5-year WMAP Ka Jupiter brightness temperature<sup>1</sup>  $T_{Jupiter} = 146.6 \pm 0.75$  K (Hill et al. 2008). We adopt a 1% in amplitude calibration uncertainty. This compares with our previous Jupiter estimate of  $T_{Jupiter} = 147.3 \pm 1.8$ K and calibration uncertainty of 1.3% (Readhead et al. 2004a).

### 3. Data Analysis

#### 3.1. Improvements to the Analysis Pipeline

We use a maximum-likelihood algorithm to calculate the power spectrum. It is based on the framework described in Myers et al. (2003) (hereafter Paper 4), but includes modifications to deal with the heterogeneous nature of the combined CBI dataset. The pipeline consists of two stages: the first stage compresses hundreds of thousands of visibilities into  $\sim 10^4$  “gridded estimators”, and calculates noise, CMB signal, and point source covariances for those estimators; the second stage calculates the maximum-likelihood spectrum from the estimators, as well as ancillary data products.

##### 3.1.1. Compressing the Data

As is the case for any compact array, the visibilities in the CBI data have highly correlated signals. To compress the data, we grid the visibilities onto a set of regularly spaced estimators in the  $(u, v)$ -plane, using the program CBIGRIDR (described in Paper 4). This compresses the few hundred thousand visibilities in a typical CBI mosaic into a few thousand estimators with essentially no loss of information, under the assumption of Gaussian noise. One of the outputs of CBIGRIDR is the matrix  $\mathbf{R}$  which maps the (Fourier-plane) sky map into estimators,

$$\Delta = \mathbf{R} \mathbf{t} + \mathbf{n}, \tag{1}$$

---

<sup>1</sup>This is the 33 GHz Rayleigh-Jeans brightness temperature of the planet minus the Rayleigh-Jeans brightness temperature of the CMB at the same frequency.

where  $\mathbf{t}$  is the Fourier transform of the true sky image,  $\mathbf{\Delta}$  is the gridded estimator vector, and  $\mathbf{n}$  is the noise component of the gridded estimator (Equation 23 of Paper 4).

The covariance of the gridded data vector  $\mathbf{\Delta}$  has signal and noise components

$$\mathbf{C} = \langle \mathbf{\Delta} \mathbf{\Delta}^\dagger \rangle = \mathbf{C}^N + \mathbf{C}^T + \mathbf{C}^{\text{scan}} + \mathbf{C}^{\text{src}} + \mathbf{C}^{\text{res}} \quad (2)$$

with contributions from noise, CMB, scan-dependent systematic errors, discrete point sources, and residual foregrounds (including a “field” of weak, confused point sources too faint for the CBI to detect individually) respectively. The  $\dagger$  operator denotes the Hermitian conjugate (complex conjugate of the matrix or vector transpose). The signal covariance  $\mathbf{C}^T$  due to the CMB temperature anisotropy signal is

$$\mathbf{C}^T = \mathbf{R} \mathbf{T} \mathbf{R}^\dagger, \quad (3)$$

where

$$\mathbf{T} \equiv \langle \mathbf{t} \mathbf{t}^\dagger \rangle. \quad (4)$$

For a Gaussian random CMB temperature field, we expect  $\mathbf{T}$  to be diagonal if  $\mathbf{t}$  is represented in spherical harmonic space, as a set of  $a_{\ell,m}$ ’s, and thus

$$\langle t_{\ell m} t_{\ell' m'} \rangle = C_\ell \delta(\ell, \ell') \delta(m, m') \quad (5)$$

encodes the CMB power spectrum  $C_\ell$ . This remains true in the small-angle approximation where

$$T_{\ell \ell'} = \langle \mathbf{t}(\mathbf{u}_\ell) \mathbf{t}^*(\mathbf{u}_{\ell'}) \rangle = C_\ell \delta(\mathbf{u}_\ell - \mathbf{u}_{\ell'}) \quad (6)$$

when  $\mathbf{t}$  is represented in Fourier space and  $\mathbf{u}$  is the 2-D wavevector, with  $\ell = 2\pi|\mathbf{u}|$  (White et al. 1999). Since  $R$  contains all the information about the effects of the instrument (such as the primary beam) and the scan strategy on the data, to combine heterogeneous datasets, we simply grid them separately and then combine their  $\mathbf{R}$ ’s.

In practice, the real and imaginary parts of the complex estimators  $\mathbf{\Delta}$  are unpacked into a real estimator vector  $\mathbf{d}$ , which is then used for the covariance analysis and calculation of the angular power spectrum.

### 3.1.2. Calculation of the Power Spectrum

The log-likelihood of Gaussian data given the model for its signal and noise given in Equation 2 is

$$\log(\mathcal{L}) = -\frac{1}{2} \mathbf{\Delta}^\dagger \mathbf{C}^{-1} \mathbf{\Delta} - \frac{1}{2} \log(|\mathbf{C}|). \quad (7)$$

The maximum-likelihood solution is the set of parameters  $q_B$  which define the theory covariance  $\mathbf{C}_T(q_B)$  such that the likelihood is maximized. We restrict ourselves to models of  $\mathbf{C}_T$  of the form  $\mathbf{C}_T = \sum q_B \mathbf{C}_B$ . One model of this form is if the  $\mathbf{C}_B$  are bins in  $\ell$ , in which case the  $q_B$  are the binned power spectrum.

We calculate the maximum-likelihood CMB power spectrum from the estimators using MPILIKELY, an MPI implementation of an algorithm described in Sievers (2003) and in Appendix A. It requires a single matrix inversion, with no additional  $n^3$  operations to calculate the gradient and approximate curvature of the likelihood at a trial spectrum. We operate on real data, as the correlations for the real and imaginary components of visibilities can be different (see Myers et al. (2003)).

The one algorithmic change we have made in MPILIKELY with the potential to affect the output power spectrum is in the numerical treatment of the projection of ground spillover and point sources with known positions. To project sources with known positions, but unknown fluxes, we form the matrix  $\mathbf{C}^{src} = \sum s_i s_i^T$ , where  $s_i$  is the expected signal from the  $i^{th}$  source, and in the past have added  $\beta \mathbf{C}^{src}$  to the noise, for large  $\beta$ . Similarly, for data taken in strips with common ground (*i.e.*, that from Sievers et al. (2007)), we calculate the matrix  $\mathbf{C}^{scan}$  expected from the ground, and have also added  $\gamma \mathbf{C}^{scan}$  with a large  $\gamma$  to the covariance. By calculating the spectrum expected from the CMB (see A.2), we find that the spectrum calculated using large but finite values for both  $\beta$  and  $\gamma$  leads to a recovered CMB power spectrum that is biased slightly low in the damping tail due to numerical artifacts in matrix inversion - see Figure 1. We now take the analytic limit as  $\beta \rightarrow \infty$  (see Appendix A.3) in MPILIKELY, and explicitly subtract the ground signal as described in Section 2, with CBIGRIDR accounting for the correlations induced by the subtraction. As can be seen in Figure 1, the ground subtraction and analytic source projection recovers an unbiased CMB power spectrum with slightly reduced errors.

### 3.2. Point Sources

Point sources are the largest astrophysical foreground in the CBI data, and are especially important at high- $\ell$ . All sources with positions that are known reliably from low frequency radio observations are removed from our power spectrum analysis; sources below this threshold require a statistical correction to the power spectrum. An accompanying paper describes a campaign of GBT and OVRO 31 GHz measurements of 2,125 NVSS sources in the CBI fields (Mason et al. 2008). As a result of this campaign we are able to much more accurately determine this correction and characterize its uncertainty.

The NRAO VLA Sky Survey (NVSS Condon et al. 1998) is a 1.4 GHz survey of the northern sky, taken to be complete down to  $S_{1.4} = 3.4$  mJy (although its nominal detection limit is 2.5 mJy). All sources with integrated flux densities above 3.4 mJy in the NVSS catalog which lie within one degree of a CBI field are projected. Source projection works well as long as the relative responses to the source are known for all data. This is true if either the source flux is constant for all observations, *or* all the data are taken in similar modes (same beam, observing strategy etc.). Because 30 GHz sources can be quite variable (e.g. Cleary et al. 2005) and the UV coverage and scan strategy changed between the two CBI data sets, we project all sources separately from the scan- and differenced-data. In other words, we project two vectors for each source, one corresponding to the source in the differenced-data, and one in the scan-data.

Sources fainter than 3.4 mJy at 1.4 GHz must be accounted for statistically. Although their sky density is statistically well characterized down to  $\mu$ Jy levels (e.g. Hopkins et al. 2003) from deep observations in a variety of fields substantially smaller than the CBI fields, these sources are the major systematic uncertainty in the power at high- $\ell$  owing to the need for a spectral extrapolation from 1.4 GHz, where their counts are well known and where they are *selected* for inclusion in the statistical term, to 31 GHz. Our analysis of GBT and OVRO 31 GHz flux density measurements in comparison with the NVSS 1.4 GHz values yields an average flux density ratio  $f \equiv S_{31}/S_{1.4} = 0.111 \pm 0.003$ ; using the low frequency counts and the full distribution of  $f$  (thus including its intrinsic width as constrained by our point source dataset) we determine a point source correction  $0.046 \pm 0.018 \text{Jy}^2/\text{Sr}$  at 31 GHz. The probability of an extreme source event giving rise to the high- $\ell$  power is also low – the highest level of power in any of more than 200 realizations of sources consistent with our data is less than  $0.1 \text{Jy}^2/\text{sr}$  (see Mason et al. (2008) for the full non-Gaussian distribution). Our new source power is nearly a factor of two lower than the earlier statistical correction used in earlier CBI analyses,  $0.08 \pm 0.04 \text{Jy}^2/\text{sr}$  (Mason et al. 2003), although consistent within uncertainties. The earlier correction was a conservative estimate based on a spectral index distribution which was biased against steep-spectrum sources. The current determination is based on simulations proceeding from mock CBI observations of the given population of residual sources through the full power spectrum pipeline. Amongst other effects this includes the effects of Poisson uncertainty in the faint source population. The full distribution of the source correction is taken into account when we estimate cosmological parameters. Further details on the point source observations and simulations are in Mason et al. (2008).

Although our GBT and OVRO data provide strong constraints on the spectral properties of the mJy-level extragalactic sources that dominate the CBI statistical correction, it is possible that at fainter flux densities the sources have different characteristics at 30 GHz. The majority of the fainter 1.4 GHz sources are expected to have steep radio spectra (Richards

2000; Condon et al. 1998), however, were there to be a substantial enhancement of sources with strongly inverted spectra between 1.4 and 31 GHz they could contribute appreciably to the excess. Mason et al. (2008) considers this scenario in detail, finding that for moderately inverted spectra ( $\alpha \sim 0.2$ ) they would need to constitute 40% of the sub-mJy population in order to fully explain the CBI excess. Were the sources to have strongly inverted spectra ( $\alpha \sim 0.8$ ), 2% of the population would be required. In contrast, in the GBT+OVRO surveys, the most steeply inverted spectrum source had  $\alpha = 0.49$  and  $< 0.1\%$  of sources had  $\alpha > 0.3$ .

### 3.3. Data Tests

The data presented here have been discussed previously in Mason et al. (2003), Pearson et al. (2003), Readhead et al. (2004a), Readhead et al. (2004b), and Sievers et al. (2007), where extensive data integrity tests were described. A number of further tests have been carried out on the data. Key results from this exercise are as follows:

1. **Dish Pointing Errors:** By analyzing beam maps on bright sources we have determined the individual antenna primary-beam pointing errors to be  $\sim 3.5'$  RMS in a single direction. We have simulated the impact of this, folding in the correlations induced by deck rotations throughout our observing strategy along with our typical  $15''$  RMS pointing errors, and find that the resulting bias in the power spectrum is  $< 9 \mu\text{K}^2$  in the highest  $\ell$  bin.
2. **Spectral Index of Projected Sources:** We have introduced systematic errors of  $\delta\alpha = \pm 1$  in the spectral index used to project sources out of the data and find that this has an effect  $< 6 \mu\text{K}^2$  in the highest  $\ell$  bin.
3. **Primary Beam:** To test the sensitivity of our power spectrum to the precise beam shape used in the analysis, we ran simulations of CBI observations using our best-fit physical model of the CBI beam (described in Pearson et al. 2003), but analyzed them with the best-fit Gaussian beam. This results in  $< 10 \mu\text{K}^2$  error at any  $\ell$ .
4. **Noise Fitting:** The way that we calculate the thermal noise for individual visibilities in our dataset results in a known  $\sim 2-6\%$  underestimate of the thermal noise variance. This underestimate depends on the observing strategy that was used. Simulations and analytic calculations of this effect have been presented in Mason et al. (2003) and Sievers (2003). To further constrain the thermal noise power spectrum, which can be a limiting factor especially at the highest  $\ell$  CBI measures, we have implemented a noise estimator after the gridding step in the analysis pipeline. This estimator splits

the 10 CBI frequency channels into two groups (*e.g.*, low-frequency/high-frequency, or even/odd channels) and fits for a thermal noise multiplier and the CMB power spectrum simultaneously. For the polarization observations this exercise yields noise spectrum multipliers of  $1.0195 + / - 0.009$  (low/high) and  $1.015 + / - 0.009$  (even/odd), in comparison with our previous best estimate of 1.0175. For the total intensity observations we find  $1.071 + / 0.008$  and  $1.071 + / - 0.008$ , in comparison with our previous best estimate of 1.057. We adopt noise variance multipliers of 1.017 and 1.071 for the polarization and total intensity observations, respectively, and an uncertainty of 0.9%.

5. **Bright Sources:** The large ( $\sim 143 \text{ deg}^2$ ) area covered by CBI makes it impossible to completely avoid bright radio sources: there are two  $S_{30} > 300 \text{ mJy}$  sources in the fields. For the observed distribution of sources in flux density ( $N(> S) \sim S^{-1}$ ), the brightest sources (or constant fractional residuals to them) will dominate the map variance. To measure the possible effect of these sources we reanalyzed the data after removing all individual CBI pointings where a point source with an apparent flux density  $S_{30} > 80 \text{ mJy}$  was evident, which removed 33 out of 259 pointings. This reduces the power spectrum by less than  $15 \mu\text{K}^2$  averaged over all  $\ell$  and shows no characteristic trend of increasing to high- $\ell$ , which would be expected of residual source contamination.
6. **Source Structure:** We project pure point source templates for the NVSS sources. The NVSS resolves  $\sim 20$  percent of the sources it detects. If the sources are resolved by the CBI, then we would expect leakage into the power spectrum. Using Montage<sup>2</sup> we mosaic the NVSS 4 deg x 4 deg maps to cover each of our CBI fields, and, zeroing out all pixels below 3 times the NVSS RMS noise level, simulate CBI observations of those maps. These observations are run through the full CBI data reduction pipeline, projecting out sources using the NVSS catalogs above 3.4 mJy. We find that our projection method removes  $>99.9\%$  of the source power, with the residual power a factor of 20 times lower than the observed CBI high- $\ell$  signal. This is a conservative estimate of the signal from source extendedness, since the high-frequency emission from AGNs tends to preferentially come from compact cores. In addition to testing the impact of source size, this is a powerful test of our data pipeline and the quality of the NVSS catalog.

---

<sup>2</sup><http://montage.ipac.caltech.edu>

## 4. Results & Interpretation

### 4.1. Power Spectrum

The final CBI total intensity power spectrum is shown in Figure 2, together with the WMAP 5-year, ACBAR, and QUaD power spectra, and best-fit tilted  $\Lambda$ CDM power spectrum model. The spectrum is given in Table 2, and full window functions and bin-bin correlations are available on-line.<sup>3</sup>

A comparison of these results with the previous CBI power spectrum is shown in Figure 3. The marked improvement is due to several factors: the inclusion of  $\sim 50\%$  more data, use of the GBT 30 GHz observations to reduce the uncertainty due to point sources, and the algorithmic improvements described in § 3.1.

At  $\ell > 1800$  there remains a clear excess of power over the expected intrinsic CMB anisotropy. This is shown in Figure 4 along with ACBAR (Reichardt et al. 2008), QUaD (Pryke et al. 2008), and BIMA (Dawson et al. 2006) measurements. To quantify this we use the Komatsu & Seljak (2002) analytic and the Bond et al. (2005) SPH simulation-based predictions of the SZ angular power spectrum. (See Section 4.3 for more details.) An amplitude for the SZ spectrum is then fit in conjunction with an amplitude for the intrinsic anisotropy spectrum, using a canonical tilted- $\Lambda$ CDM model<sup>4</sup> as a shape. The templates are calculated with  $\sigma_8 = 0.8$  and  $\Omega_b h = 0.0321$ . This results in a  $3.1\sigma$  detection of power in excess of the intrinsic anisotropy (a best-fit scaling of  $3.5 \pm 1.3$  of the nominal KS template). The SPH template has a best-fit scaling of  $5.4 \pm 1.8$  and a  $3.4\sigma$  detection significance. The detection significances are calculated using  $\sqrt{-2\delta \log(\mathcal{L})}$ , where the likelihood difference is between the best-fit CMB-only shaped model and the best-fit CMB+template model. We show the total power spectrum including the contribution of the best-fit SZ spectrum by the *dashed* lines in Figure 4. Of note is the marked change in the magnitude of the SZ power spectrum between 30 and 150 GHz, and the fairly broad contribution of clusters down to as low as  $\ell \sim 1000$ .

Since the secondary SZ anisotropy will be highly non-Gaussian, uncommon structures in the  $\sim 4 \text{ deg}^2$  of “deep” CBI pointings could bias the power spectrum (although the statistical weight of the wide, shallow area is about 2.5 times of that of the deep data). We re-ran the power spectrum extraction both *excluding* the deep field data from the analysis, and using

---

<sup>3</sup><http://www.astro.caltech.edu/~tjp/CBI/data/index.html>

<sup>4</sup>Flat,  $\Omega_b h^2 = 0.0223$ ,  $\Omega_{CDM} = 0.108$ ,  $\tau = 0.087$ ,  $n_s = 0.96$ , and including the effects of gravitational lensing. No SZ contribution is included, as that is handled separately.

*only* the deep data. The results are shown in Figure 5. While the error bars are increased by  $\sim 25\%$ , the amplitude of the power spectrum at  $\ell > 1000$  is not reduced, indicating that the small-scale excess power is not a peculiar property of the deep fields observed by CBI. An assessment of the cosmic variance in the high- $\ell$  CBI power spectrum, under the assumption that the dominant signal over intrinsic anisotropy is due to SZ clusters, is presented in § 4.3.

Power spectra from the individual CBI fields are shown in Figure 6. To increase the signal-to-noise ratio a coarser binning has been used. Each of the CBI mosaics shows an excess of at least  $0.7\sigma$ , with levels of (  $2.7 \pm 2.6$ ,  $7.6 \pm 2.9$ ,  $2.6 \pm 2.3$ , and  $1.6 \pm 2.2$  ) above the CMB using the  $\sigma_8 = 0.8$  KS template for the (02, 08, 14, 20)-hour mosaics. The individual fields are all consistent with the same excess level (reduced  $\chi^2 = 1.01$  per dof), with the most discrepant field  $1.6\sigma$  away from the mean.

The CBI data by themselves cannot determine the source of the excess. In particular, they cannot distinguish an SZ foreground from point sources (if one fits for a point source and an SZ amplitude simultaneously, the power spectra are sufficiently similar that the error bars more than triple). If instead of an SZ template, we model the excess with a point source-like template, we find its total amplitude is  $0.180 \pm 0.052 \text{Jy}^2/\text{sr}$  above the expected contribution from unresolved sources of  $0.046 \text{Jy}^2/\text{sr}$ . To high accuracy, the best-fit SZ excess level is linearly dependent on the input source level. For the KS template, the best-fit SZ amplitude is  $q_{sz} = 4.59 - 24.7 \times q_{iso}$  where  $q_{sz}$  is in units of the predicted SZ signal for  $\sigma_8 = 0.8$  and  $q_{iso}$  is the faint source contribution in  $\text{Jy}^2/\text{sr}$ . One can use this relation to ask how different mean source levels would affect the excess: a value of 0.186 for  $q_{iso}$  would make the high- $\ell$  excess disappear, a value of 0.146 would make the best-fit CBI value be equal to the predicted KS level, and a value of 0.096 would make the best-fit CBI value be within  $1-\sigma$  of the predicted KS level.

## 4.2. Diffuse Foregrounds

While on small scales, point sources are the largest 30 GHz foreground, on larger scales ( $\gtrsim 1$  degree), diffuse foregrounds dominate. At frequencies of  $\sim 30$  GHz, the major known diffuse Galactic foregrounds are synchrotron radiation and free-free emission. Vibrational (thermal) dust emission is negligible at frequencies below  $\sim 50$  GHz. However, there is considerable evidence for an additional component which is closely correlated with FIR dust maps and that appears to dominate the spectrum in the range  $\sim 10\text{--}50$  GHz (Leitch et al. 1997; Banday et al. 2003; de Oliveira-Costa et al. 2004; Finkbeiner 2004; Davies et al. 2006; Bonaldi et al. 2007; Hildebrandt et al. 2007; Dobler & Finkbeiner 2008a,b). Both the COBE-DMR and WMAP datasets have shown that the high latitude

sky is dominated by such a foreground closely linked with dust emission, usually traced in the FIR ( $\lambda \sim 100 \mu\text{m}$ ). The most popular candidate for this anomalous component is the so-called “spinning dust” emission (Draine & Lazarian 1998a,b; Ali-Haïmoud et al. 2008), but the situation is far from clear.

Whether or not the dominant diffuse emission is spinning dust or flat-spectrum synchrotron is not of great importance in the context of this paper. However, we need to quantify the level at which diffuse foregrounds are present in our data. We use the fact that the FIR maps are a good tracer of the foreground morphology at these frequencies. In the WMAP data at K and Ka-bands (23 and 33 GHz, respectively), there is a strong correlation with the 100  $\mu\text{m}$  Schlegel et al. (1998) map. If the emissivity of the dust emission is roughly constant for a given region, cross-correlation between the FIR map and CBI data provides a very sensitive method to detect such emission. Furthermore, IRAS data have adequate resolution to cover the angular scales measured by CBI.

We simulated CBI data based on the Schlegel et al. (1998) 100  $\mu\text{m}$  map as our foreground “reference” map. The 100  $\mu\text{m}$  maps were converted to CBI visibilities using the MOCKCBI software based on the real observed visibility data sets. To convert to the approximate signal levels expected at 30 GHz, we took a typical dust emissivity at high Galactic latitude of 10  $\mu\text{K}/(\text{MJy}/\text{sr})$  (Banday et al. 2003; Davies et al. 2006). Although the emissivity can vary by a factor of a few over the sky, it provides an initial guess for the amplitude of the signal *i.e.*, we expect a cross-correlation coefficient of  $\sim 1$  based on previous data on larger angular scales. We also repeated the analysis using  $\text{H}\alpha$  data from the compilation of Finkbeiner (2003).  $\text{H}\alpha$  is known to be good tracer of free-free emission at high Galactic latitudes where dust extinction is small (Dickinson et al. 2003). We scaled the  $\text{H}\alpha$  template by 5.83  $\mu\text{K}$  per Rayleigh, which is the expected value at 31GHz, assuming  $T_e \approx 8000 \text{ K}$  (Dickinson et al. 2003).

The simulated foreground visibilities were fitted to the CBI data using the template-fitting method of Appendix A.5. For the dust template of Schlegel et al. (1998), we found a combined correlation coefficient of  $1.18 \pm 0.53$  ( $2.2\sigma$ ) for the entire dataset. This suggests that a very small level of contamination from Galactic emission might exist in the CBI data, at a level similar to those observed at larger angular scales (Banday et al. 2003; Davies et al. 2006). The fluctuation power  $C_\ell$  in the FIR dust scale as  $C_\ell \propto \ell^{-3}$ , (Gautier et al. 1992), thus the power will be mostly at large angular scales. For the  $\text{H}\alpha$  template we find a combined correlation coefficient of  $0.78 \pm 0.58$ . For both foreground templates, we find a negligible impact on the power spectrum, with the high- $\ell$  excess changing by less than 1%. The emissivity factor is close to what is expected at high latitudes and indicates that the CBI fields are relatively low in foregrounds on angular scales  $< 1^\circ$ . This is also supported by

the field-by-field data splits (§4.1): all the independent fields give consistent power spectra.

### 4.3. Cosmological Parameters

We can place constraints on the standard parameters of tilted  $\Lambda$ CDM cosmology by fitting a range of model spectra to the observed CMB (and other) data. Model spectra were generated by CAMB (Lewis et al. 2000) and the parameter constraints determined by a modified version of the Monte-Carlo Markov Chain code, COSMOMC (Lewis & Bridle 2002). For all parameter runs, we take into account the effects of CMB lensing, and assume a prior that the universe is spatially flat. To capture the non-Gaussian nature of the CBI’s power spectrum, we use the offset-lognormal approximation of Bond et al. (2000) in parameter analysis. To convert model spectra to predicted CBI bandpowers, we evaluate the window functions with a spacing of  $\delta\ell = 20$ , and use cubic Hermitian polynomial interpolation between the measured points.

We extend the treatment of the SZ foreground relative to previous analyses (Bond et al. 2005; Readhead et al. 2004a). We assume the angular power spectrum from clusters scales in a simple analytic fashion:  $\propto \sigma_8^7 (\Omega_b h)^2$  (Bond et al. 2005; Komatsu & Seljak 2002). We have explored two sets of SZ templates:

1. Semi-analytic templates from Komatsu & Seljak (2002) (the KSSZ template), updated to include the effect of  $\sigma_8$  on the shape of the SZ power spectrum (E. Komatsu, private communication). The dependence of the shape on  $\sigma_8$  is found to be minimal.
2. Power spectra from tree-SPH simulations described in Bond et al. (2005) (the SPH template).

The SPH template has relatively less power than KSSZ for fixed cosmological parameters, and rises more quickly with  $\ell$ . Unless stated otherwise the KSSZ template is used in all parameter analysis. Also unless otherwise indicated, all runs use the full  $\ell$  range of data and explicitly model the SZ foreground. Based on a comparison of these theoretical templates, we estimate that for a given background cosmology there is a factor of  $\sim 2$  uncertainty in the SZ power spectrum. This corresponds to a  $\sim 10\%$  systematic uncertainty in  $\sigma_8$ . Because of this we do *not* link the SZ spectra to the background cosmology, *e.g.*, through  $\Omega_b$  or  $\sigma_8$ . Rather we use an independent parameter  $\sigma_8^{SZ}$  to describe the amplitude of the SZ power spectrum and to index the family of shaped SZ power spectra.

Table 3 shows the marginalized individual parameter results for an analysis including WMAP 5-year (Nolta et al. 2008; Dunkley et al. 2008) and CBI data, using both SZ tem-

plates. This includes a marginalization over the uncertainty in the residual point source power spectrum using the distribution determined from the simulations in § 3.2. Table 4 contains the same parameters, but with the addition of more CMB data to CBI and WMAP: ACBAR (Reichardt et al. 2008), BIMA (Dawson et al. 2006), VSA (Dickinson et al. 2004), Boomerang (Montroy et al. 2006; Jones et al. 2006), QUAD (Ade et al. 2008, adopting their “pipeline 1” spectrum), and both CBI and DASI polarization data (Sievers et al. 2007; Leitch et al. 2004). We henceforth refer to this data combination as CMBall. The choice of SZ template has an impact on the value of  $\sigma_8$  inferred from the primary fluctuations - the Bond et al. (2005) template gives  $\sigma_8$  values that are systematically higher by about 0.015 than the Komatsu & Seljak (2002) template. This is because the KSSZ template is flatter than the SPH template, so for fixed observed power at  $\ell \sim 2000$ , KSSZ will remove *more* power in the region of the third peak, dropping  $\sigma_8$ . Our values of  $\sigma_8$  are also lower than those in Dunkley et al. (2008) where the level of the KSSZ template is capped at twice the level predicted for a  $\sigma_8 = 0.8$  universe. We allow the amplitude to float freely, and the CBI data set the level to be around 2.5 times the  $\sigma_8 = 0.8$  prediction, again resulting in more power being removed from the third peak and a lower primary  $\sigma_8$  value.

The values of  $\sigma_8$  inferred from the high- $\ell$  power spectrum are  $\sigma_8^{SZ} = 0.910 \pm 0.064$  for CBI+WMAP5 and  $\sigma_8^{SZ} = 0.922 \pm 0.047$  for CMBall. As a point of comparison, using the SPH template, we find  $\sigma_8^{SZ} = 1.015 \pm 0.060$  for CBI+WMAP5 and  $\sigma_8^{SZ} = 0.977 \pm 0.049$  for CMBall. CMBall has a (slightly) higher inferred  $\sigma_8^{SZ}$  than CBI+WMAP5 for the KSSZ template, whereas it has a lower one for the SPH template. This is due to the BIMA data falling above the CBI prediction for the relatively flat KSSZ template, while they fall below the CBI prediction for the SPH template. We find that CBI, ACBAR, and BIMA are consistent with each other if the high- $\ell$  excess is due to SZ - see Figure 7 for full MCMC chains comparing the three experiments using both SZ templates. For comparison with other experiments, we give the best-fit CBI excess level (from Table 3) for the two templates at selected  $\ell$  and frequencies. The results are summarized in Table 5.

When we extend the  $\Lambda$ CDM model to include tensor modes, we find no detection of them:  $r < 0.32$  (95%) for CMBall, where  $r$  is the tensor-to-scalar power ratio at the pivot wavenumber  $0.05 h \text{ Mpc}^{-1}$ .

We have explored the potential impact of cosmic strings in the CMB using a string template of Pogosian et al. (2008). We treat the string contribution as a template of fixed shape added to the power spectrum, and allow its overall amplitude  $q_{string}$  to float, just as we have for the SZ templates with overall parameter  $q_{SZ}$ . We re-emphasize the Pogosian et al. (2008) caution that the power spectrum from strings is not uniquely determined and its shape depends on the details of the string properties. While no combination of CMB data

detects cosmic strings, the addition of high- $\ell$  CMB data adds a significant constraint to the maximum allowed string amplitude: the 95% string upper limit from CMBall is 65% of the limit from WMAP5 alone (see Fig. 8). The high- $\ell$  data constrain strings because the power spectrum from them generically falls off more slowly with  $\ell$  than that from the adiabatic fluctuations since the string fluctuations are not subject to Silk damping (Pogosian et al. 2008). The amplitude  $q_{string} \propto (G\mu)^2$  can be expressed in terms of the string tension  $\mu$  times Newton’s constant  $G$ . The limits on  $G\mu$  (which scales like the square root of the power spectrum amplitude) are  $G\mu < 3.4 \times 10^{-7}$  for WMAP5 only, and  $G\mu < 2.8 \times 10^{-7}$  for CMBall. With WMAP only, the string amplitude is highly degenerate with  $n_s$  (e.g., Battye et al. (2006), see Fig. 8), and there is no longer a “detection” of  $n_s < 1$ , rather we obtain  $n_s = 0.972 \pm 0.018$  with a 95% upper limit of 1.007. The addition of the high- $\ell$  CMB breaks this degeneracy, and  $n_s$  remains less than one with high significance: we obtain  $n_s = 0.961 \pm 0.015$  with a 95% upper limit of 0.990.

We find that the addition of the CBI data have a strong impact on the running of the scalar spectral index,  $\frac{dn_s}{d\log k}$  (evaluated at a pivot wavenumber of  $0.05 h \text{ Mpc}^{-1}$ ). For the KSSZ template, we find  $\frac{dn_s}{d\log k} = (-0.041 \pm 0.031, -0.048 \pm 0.028, -0.066 \pm 0.022)$  for ( WMAP5, WMAP5+CBI, CMBall), respectively. For the SPH SZ template, we find  $\frac{dn_s}{d\log k} = (-0.039 \pm 0.030, -0.042 \pm 0.027, -0.059 \pm 0.022)$  for ( WMAP5, WMAP5+CBI, CMBall), respectively. Thus, with CMBall, the running of the spectral index is a 2.76- $\sigma$  “detection” for the SPH template, and 3.03- $\sigma$  one for the KS template. The detection is substantially driven by the high values obtained for the SZ signal. When the allowed SZ level is capped at twice the nominal KS value, we find that limits on  $\frac{dn_s}{d\log k}$  for CMBall are  $-0.048 \pm 0.021$  and  $-0.043 \pm 0.021$  for the KS and SPH templates, around 2- $\sigma$  detections (see Fig. 9). We stress that the inferred value of  $\frac{dn_s}{d\log k}$  depends not only on the amplitude of the SZ signal, but somewhat on its shape as well, hence the difference in  $\frac{dn_s}{d\log k}$  between the two templates.

Since clusters are compact sources, the distribution from field to field will not be Gaussian. We have assessed the effect on the sample variance in the SZ cluster power spectrum for the CBI coverage region using the simulated maps of White (2003). These consist of 10 maps of the thermal SZ effect, each  $10^\circ \times 10^\circ$  in size. These are calculated using large N-body simulations in a  $\Lambda$ CDM cosmology with  $\sigma_8 = 1$ . The pressure profiles of the clusters were made assuming the gas density follows the dark matter density, and the temperature is isothermal and proportional to  $M_{halo}^{2/3}$  (Schulz & White 2003). The SZ maps are line-of-sight integrations of these 3D pressure configurations. Fake observations of these fields are constructed using the real CBI  $uv$  coverage and per-visibility noise levels and they are run through our power spectrum extraction. The thermal SZ power spectrum at  $\ell > 1800$  emerging from this analysis has a mean level of  $\sim 200 \mu\text{K}^2$ . When only the CBI deep fields are used we find an RMS in the SZ power spectrum of  $\sim 100 \mu\text{K}^2$ , that is a fractional scatter of about

50% in the (noiseless) spectra. When the full CBI sky coverage is probed instead of just the deep fields, we find a fractional scatter in the SZ spectrum to be 21%. The 21% scatter could be driven by non-Gaussian errors in the deep fields. To test this, we excluded the deep fields from the CBI mosaics and repeated the analysis. We found that the fractional scatter dropped to 19%, hence the deep fields do not drive up the variance of the total result by a substantial amount. We expect that the non-Gaussian component will be quite sensitive to  $\sigma_8$  since the number of clusters drops dramatically as  $\sigma_8$  is dropped, increasing the Poisson fluctuations. Thus the sample variance in the SZ spectrum depends heavily on the value of  $\sigma_8$ , and since the sample variance errors are highly correlated between multipole bins, these results have not been fed into further analysis, but should be taken as indicative.

## 5. Summary

We have presented the total intensity power spectrum resulting from five years of dedicated CBI observations and campaigns of point source foreground observations with the OVRO 40-m and the GBT. The OVRO and GBT data allow us to greatly improve our estimate of the power from faint 30 GHz radio sources. On its own, the CBI cannot distinguish between power spectra from point sources and from other sources such as the SZ effect from galaxy clusters, and so these supporting observations are essential. Our data support the existence of excess power above the primary CMB on small angular scales at  $\sim 3\sigma$ , and are the most sensitive constraints to date on the statistical SZ cluster foreground. In extensive testing, we find no evidence of any instrumental systematic effect capable of giving rise to the excess. By running the NVSS maps (with all pixels below three times the NVSS RMS noise zeroed out) through the CBI pipeline, we find that our source treatment rejects  $>99.9\%$  of the power in known sources. This test confirms the quality of the NVSS catalogs, the validity of the projection of known sources, and the insensitivity of the CBI to extended sources. If the excess is due to the SZ effect, we find that other data, notably ACBAR and BIMA, are consistent with the excess seen by CBI. For two different SZ spectral templates, we find that the inferred  $\sigma_8$  from the excess is marginally inconsistent with those derived from the primary fluctuations,  $0.922 \pm 0.047$  and  $0.988 \pm 0.049$  vs.  $0.769 \pm 0.031$  and  $0.784 \pm 0.030$ . To determine definitively the implications of the observed small-scale excess power further theoretical work is needed. We find that high- $\ell$  data break the degeneracy between the tilt of the spectral index  $n_s$  and potential contributions from cosmic strings. From running n-body simulations through the CBI pipeline, we find that the scatter in the expected level of the signal from clusters due to their non-Gaussian nature is about 20%.

The CBI has been supported by funds from the National Science Foundation under

grants AST 9413935, 9802989, 0098734, and 0206416, by the California Institute of Technology, by Maxine and Ronald Linde, Cecil and Sally Drinkward, Barbara and Stanley Rawn Jr., Rochus Vogt, the Canadian Institute for Advanced Research, and by the Kavli Institute for Cosmological Physics. We thank E. Komatsu for providing us with additional tabulations of SZ power spectrum templates. All computations were performed on the Canada Foundation for Innovation funded CITA Sunnyvale cluster. Part of the research described in this work was carried out at the Jet Propulsion Laboratory, California Institute of Technology, under a contract with the National Aeronautics and Space Administration. The National Radio Astronomy Observatory is a facility of the National Science Foundation operated under cooperative agreement by Associated Universities, Inc. LB and JM acknowledge support from Chilean Center of Excellence in Astrophysics and Associated Technologies (PFB 06), and from Chilean Center for Astrophysics FONDAF 15010003. This research made use of Montage, funded by the National Aeronautics and Space Administration’s Earth Science Technology Office, Computation Technologies Project, under Cooperative Agreement Number NCC5-626 between NASA and the California Institute of Technology. Montage is maintained by the NASA/IPAC Infrared Science Archive.

## REFERENCES

- Ade, P., Bock, J., Bowden, M., Brown, M. L., Cahill, G., Carlstrom, J. E., Castro, P. G., Church, S., Culverhouse, T., Friedman, R., Ganga, K., Gear, W. K., Hinderks, J., Kovac, J., Lange, A. E., Leitch, E., Melhuish, S. J., Murphy, J. A., Orlando, A., Schwarz, R., O’Sullivan, C., Piccirillo, L., Pryke, C., Rajguru, N., Rusholme, B., Taylor, A. N., Thompson, K. L., Wu, E. Y. S., & Zemcov, M. 2008, *ApJ*, 674, 22
- Ali-Haïmoud, Y., Hirata, C. M., & Dickinson, C. 2008, ArXiv e-prints
- Banday, A. J., Dickinson, C., Davies, R. D., Davis, R. J., & Górski, K. M. 2003, *MNRAS*, 345, 897
- Battye, R. A., Garbrecht, B., & Moss, A. 2006, *Journal of Cosmology and Astro-Particle Physics*, 9, 7
- Bonaldi, A., Ricciardi, S., Leach, S., Stivoli, F., Baccigalupi, C., & de Zotti, G. 2007, *MNRAS*, 382, 1791
- Bond, J. R., Contaldi, C. R., Pen, U.-L., Pogosyan, D., Prunet, S., Ruetalo, M. I., Wadsley, J. W., Zhang, P., Mason, B. S., Myers, S. T., Pearson, T. J., Readhead, A. C. S., Sievers, J. L., & Udomprasert, P. S. 2005, *ApJ*, 626, 12

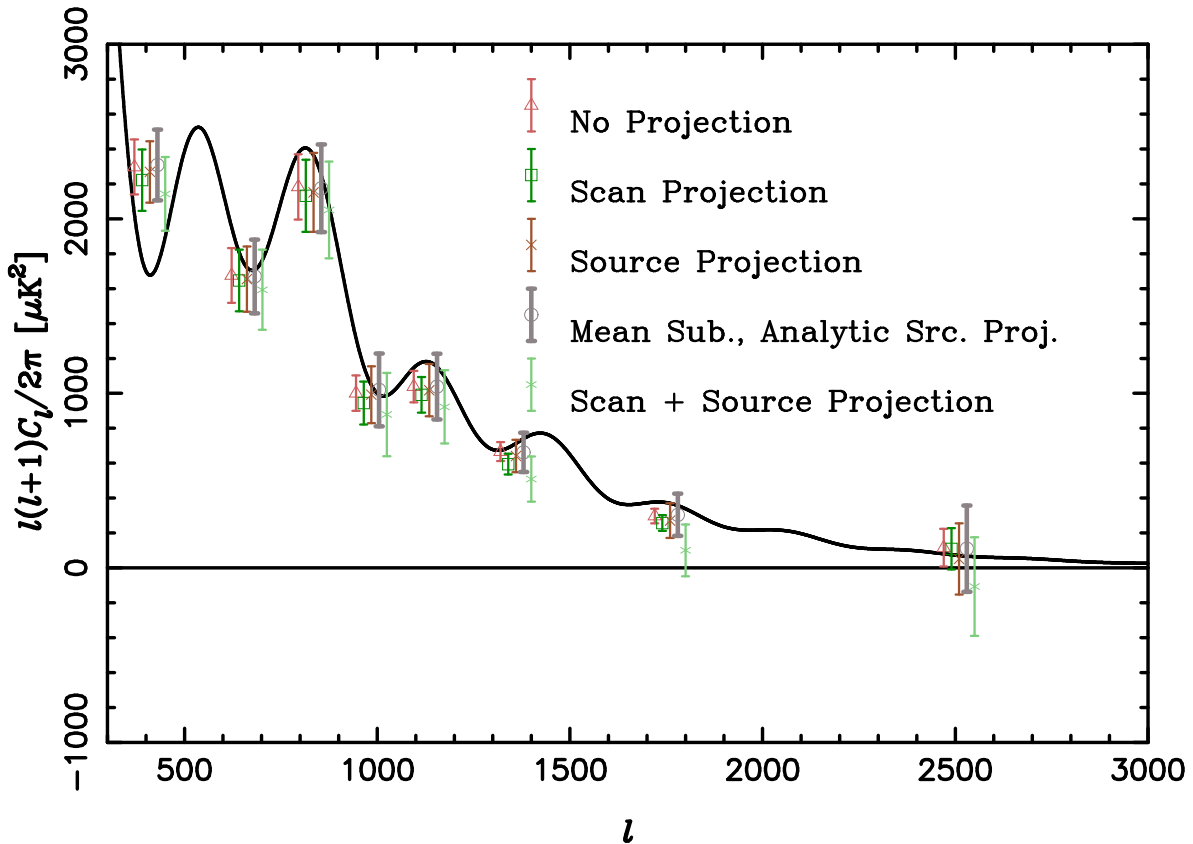


Fig. 1.— Effects of projections on the expected spectrum from the CBI strips. The red triangles show the expected spectrum from just the TT part of the CBI polarization data with no removal of ground or sources. The green squares show the expected spectrum when the scan mean (which contains the ground signal) is projected out. The red X’s show the spectrum when only the sources are projected. The green X’s show the spectrum when both sources and ground are projected - there is a significant bias downwards in the spectrum. The grey circles show the the same spectrum when the scan mean is subtracted rather than projected, and the sources are projected using the numerically stable method of Appendix A. The black curve is the input CMB spectrum. This method keeps the covariance matrix better conditioned, so it is less susceptible to roundoff errors in the inversion. These spectra are fit to the theoretical CMB+noise signal matrix using the techniques described in Appendix A.2, which is equivalent to averaging over all possible noise and signal simulations. The CBI differenced data from Readhead et al. (2004a) were already effectively scan-mean subtracted, and so are not included here.

Bond, J. R., Jaffe, A. H., & Knox, L. 1998, Phys. Rev. D, 57, 2117

Bond, J. R., Jaffe, A. H., & Knox, L. E. 2000, ApJ, 533, 19

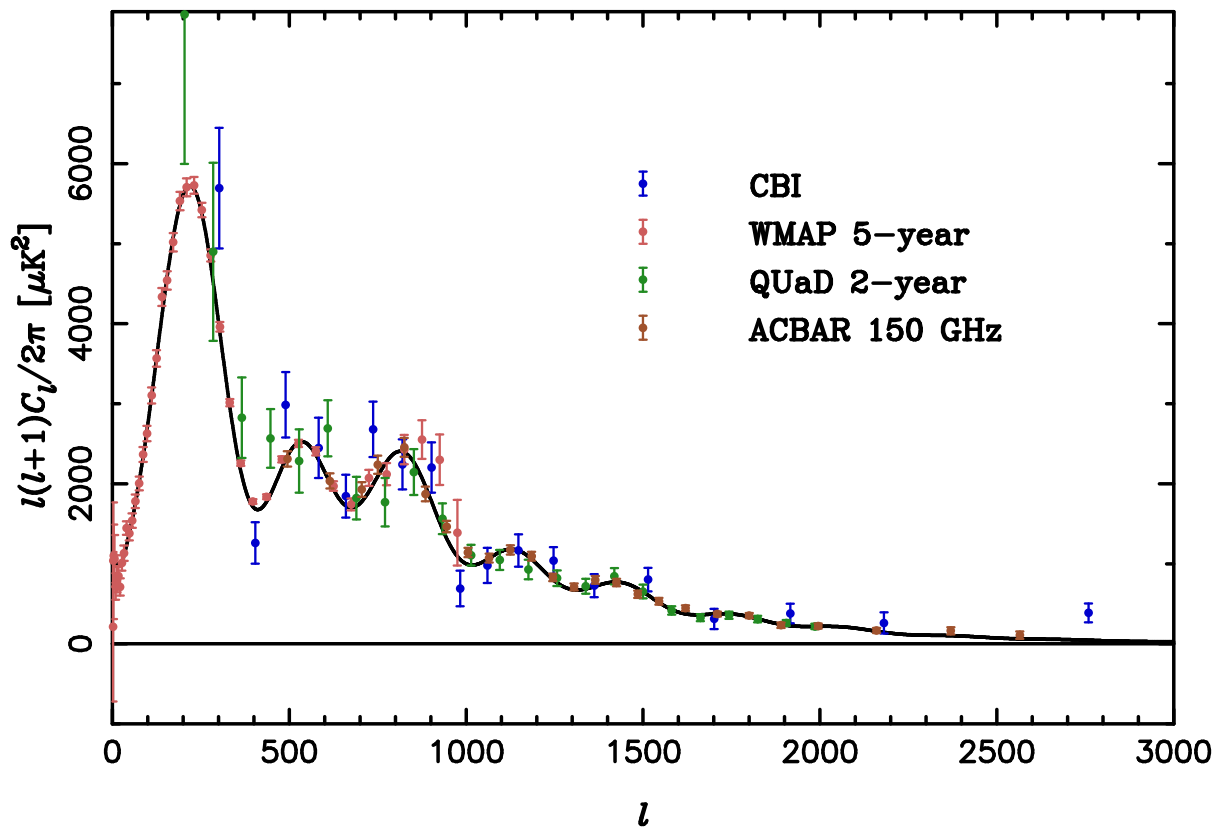


Fig. 2.— CBI total intensity power spectrum. The blue points are the CBI power spectrum in this work, given in text form in Table 2. The salmon points are the WMAP 5-year spectrum (Nolta et al. 2008). The green points are the QUaD 2-year spectrum (Pryke et al. 2008). The burnt sienna points are the ACBAR 150 GHz spectrum (Reichardt et al. 2008). The full CBI spectrum, including bin correlations and window functions, is available online.

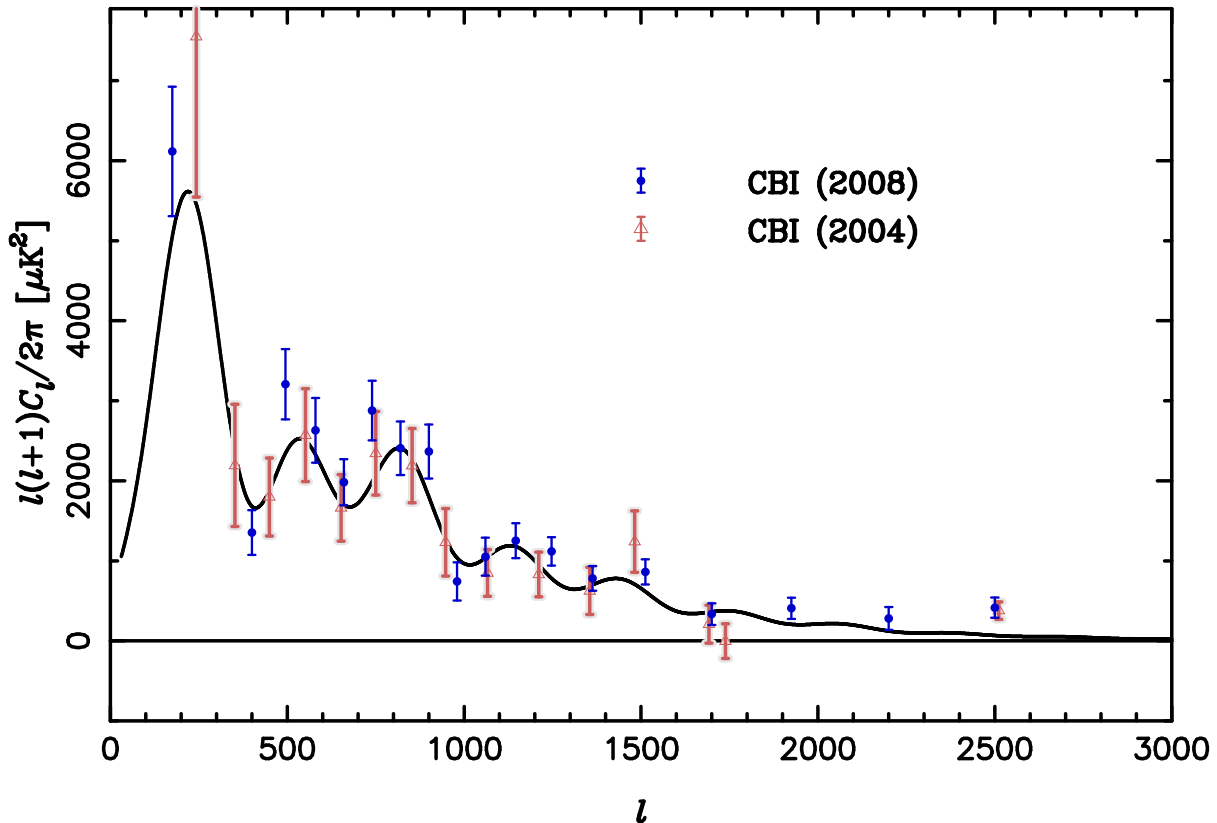


Fig. 3.— A comparison of the CBI 5-year power spectrum, including results from the GBT 30 GHz survey, with the two-year CBI power spectrum of Readhead et al. (2004a). Note the changed finer binning at high  $\ell$  for the power spectrum from the 5-year data. The window function of the Readhead et al. (2004a) highest- $\ell$  bin extends from  $\ell \sim 2000$  to  $\ell \sim 3500$ . Note that the error bar on that very big bin is about the same as for the last of the finer bins, in spite of the large Readhead et al. (2004a) bin being broken up into three distinct bins in this work. The main reasons for the improvement in the spectrum is the factor of two more data, and the development of analysis techniques that allowed us to combine these disparate datasets. In the damping tail, the new spectrum is about a factor of two improvement over Readhead et al. (2004a).

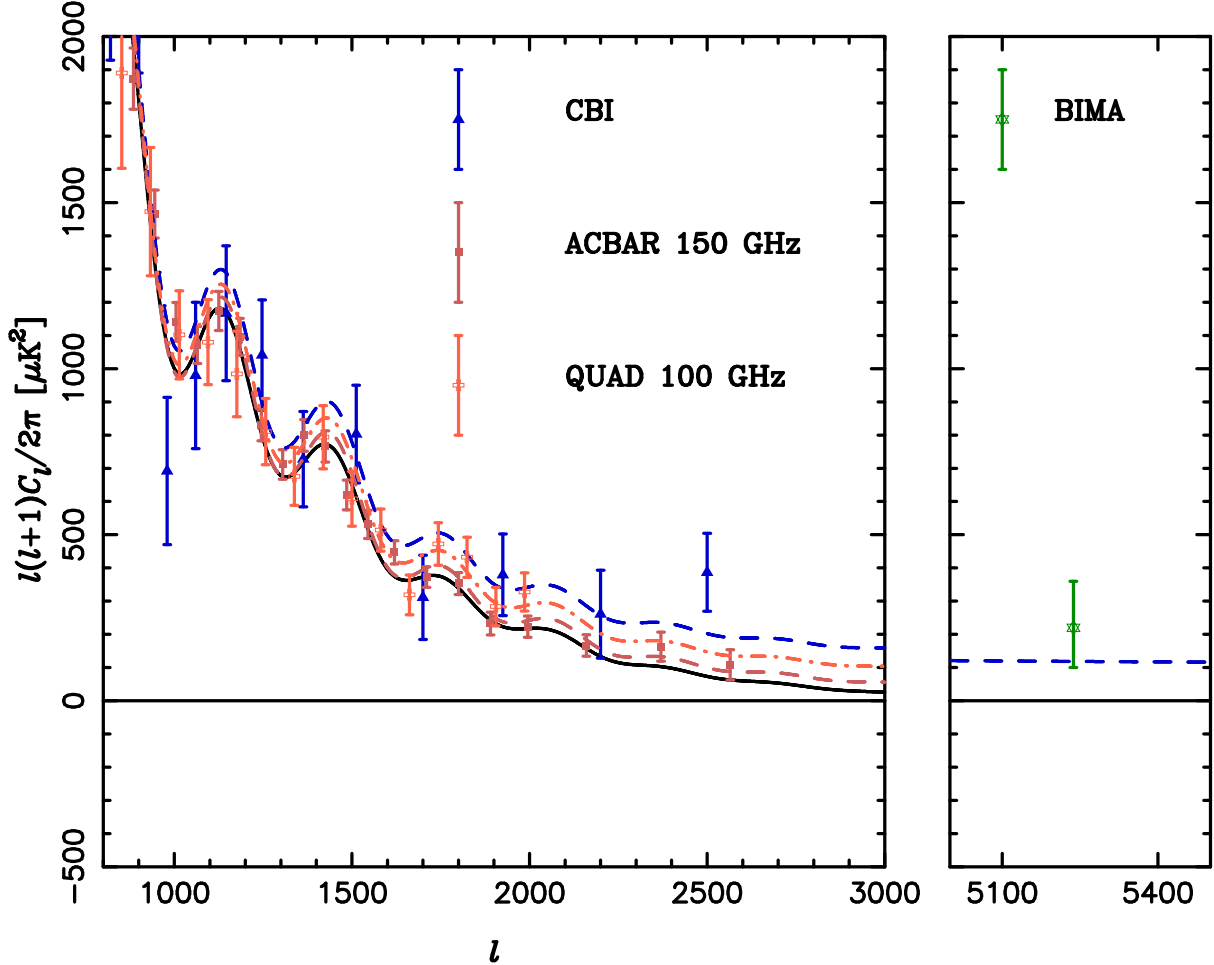


Fig. 4.— The CBI, ACBAR, QUaD, and BIMA power spectra at small angular scales are contrasted. The solid black line shows the tilted  $\Lambda$ CDM model from Section 4.1 for the CMB primary anisotropies. The dashed lines include the contribution of secondary SZ anisotropy using the model of Komatsu & Seljak (2002) with the best-fit template scaling of 3.5 (in bandpower) that we have determined using only the CBI data. The SZ plus primary anisotropy power combination at 30 GHz is the blue-dashed line. Note that, apart from fitting the CBI power spectrum, it passes through the BIMA point at  $\ell \sim 5300$  (Dawson et al. 2006). We have also forecast the level for SZ plus primary anisotropies at 150 GHz (red dashed line) and 100 GHz (orange dot-dash line). These are compared with the power spectra of ACBAR (Reichardt et al. 2008) and QUaD (Pryke et al. 2008).

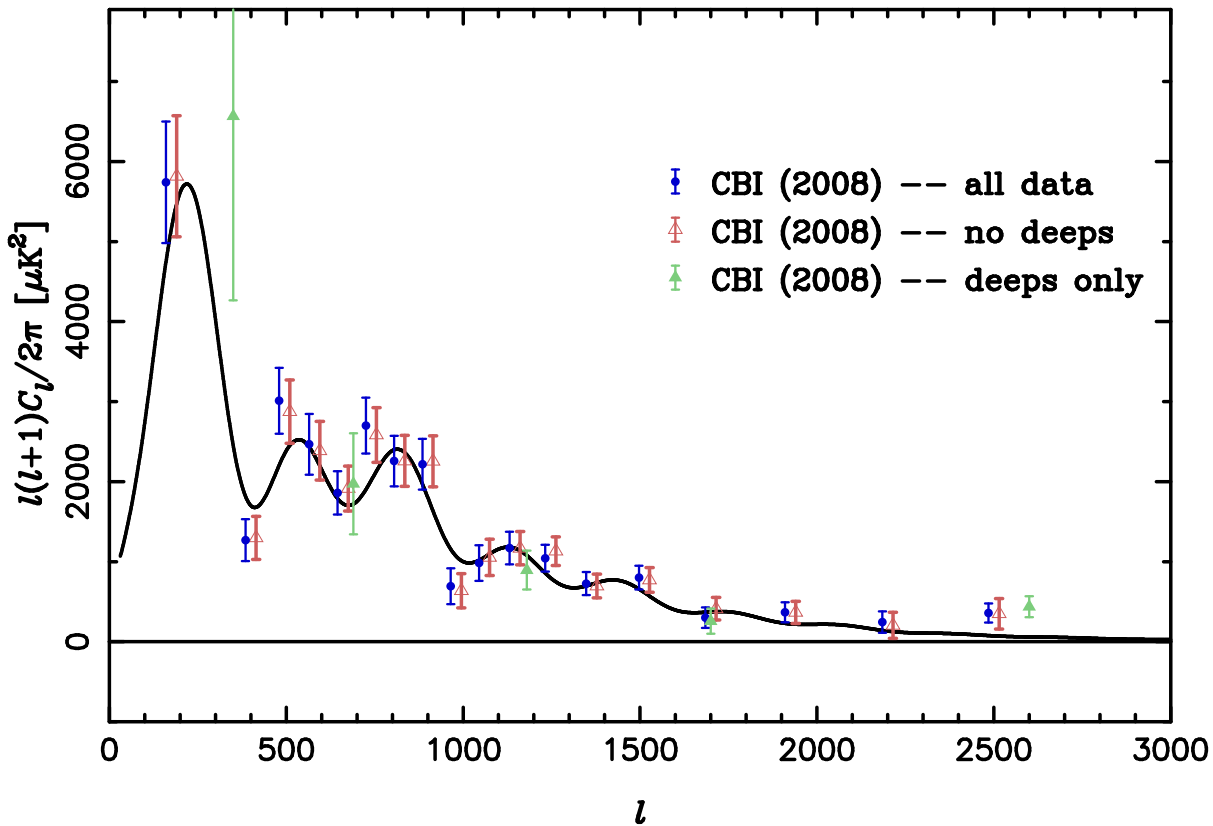


Fig. 5.— A comparison of the power spectrum obtained from all CBI TT data with that obtained when the deep fields are excluded, and with that obtained when only the deep fields are used. Although the error for the no-deeps at  $l \sim 2500$  is larger, and consistent with no excess at the  $\sim 1 - \sigma$  level, the overall mean amplitude is about the same as for the deep-only case. The all-data and no-deeps spectra are at the same  $l$ , but have been offset for clarity.

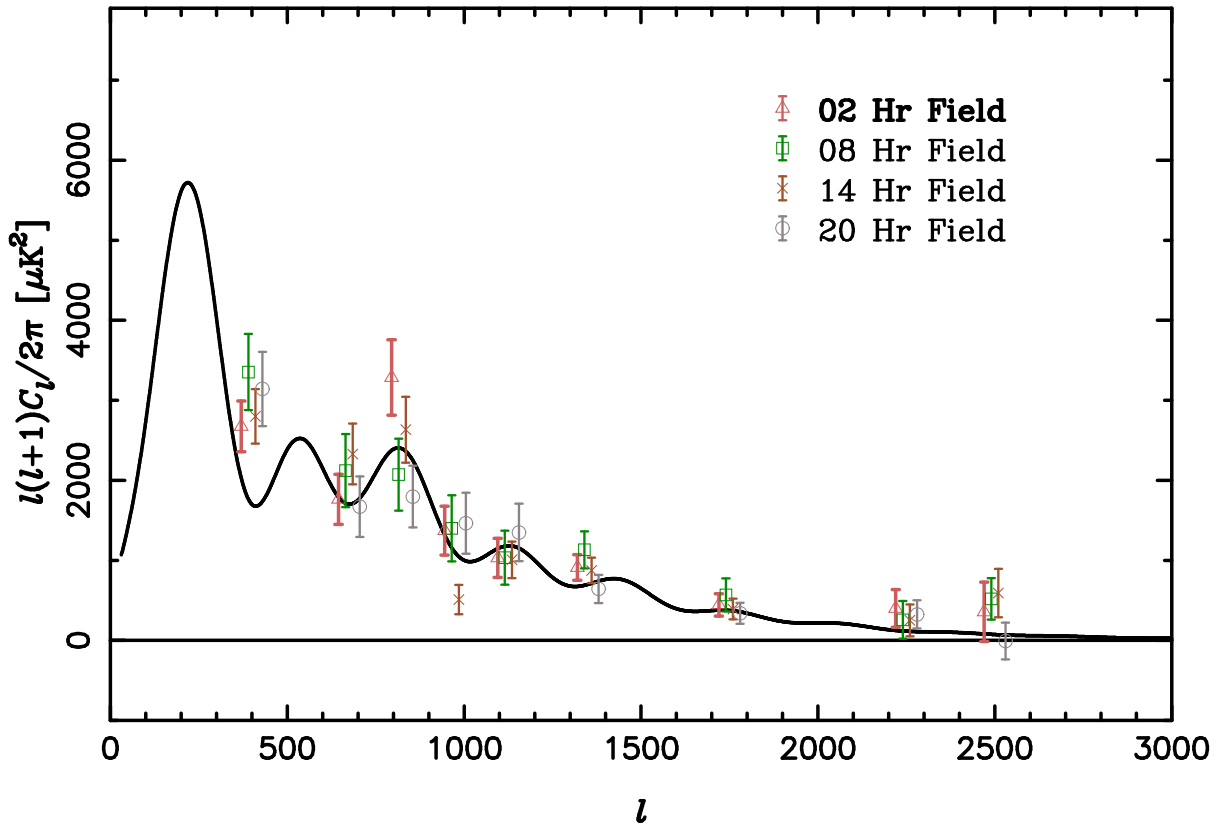


Fig. 6.— Power spectra from individual CBI fields show how the bandpowers fluctuate from field to field. The individual fields are all consistent with each other, and each sees power above the CMB. The spectra are staggered in  $l$  for clarity in plotting.

Table 1: CBI Fields

name	R.A. (J2000)	Dec (J2000)	Dimensions	Ground Removal Strategy
02h	02 : 50 : 00	−01 : 30 : 00	$5^\circ \times 6^\circ$	8-min differences
08h-deep	08 : 44 : 40	−03 : 10 : 00	$0.75^\circ \times 0.75^\circ$	8-min differences
14h	14 : 50 : 00	−02 : 30 : 00	$5^\circ \times 5^\circ$	8-min differences
14h-deep	14 : 42 : 00	−03 : 50 : 00	$0.75^\circ \times 0.75^\circ$	8-min differences
20h	14 : 50 : 00	−02 : 30 : 00	$5^\circ \times 5^\circ$	8-min differences
20h-deep	20 : 48 : 40	−03 : 30 : 00	$0.75^\circ \times 0.75^\circ$	8-min differences
02h-pol	02 : 49 : 30	−02 : 52 : 30	$5^\circ \times 5^\circ$	scan mean subtraction
08h-pol	08 : 47 : 30	−02 : 47 : 30	$5^\circ \times 5^\circ$	scan mean subtraction
14h-pol	14 : 45 : 30	−04 : 07 : 30	$5^\circ \times 5^\circ$	scan mean subtraction
20h-pol-deep	20 : 49 : 30	−03 : 30 : 00	$5^\circ \times 0.75^\circ$	scan mean subtraction

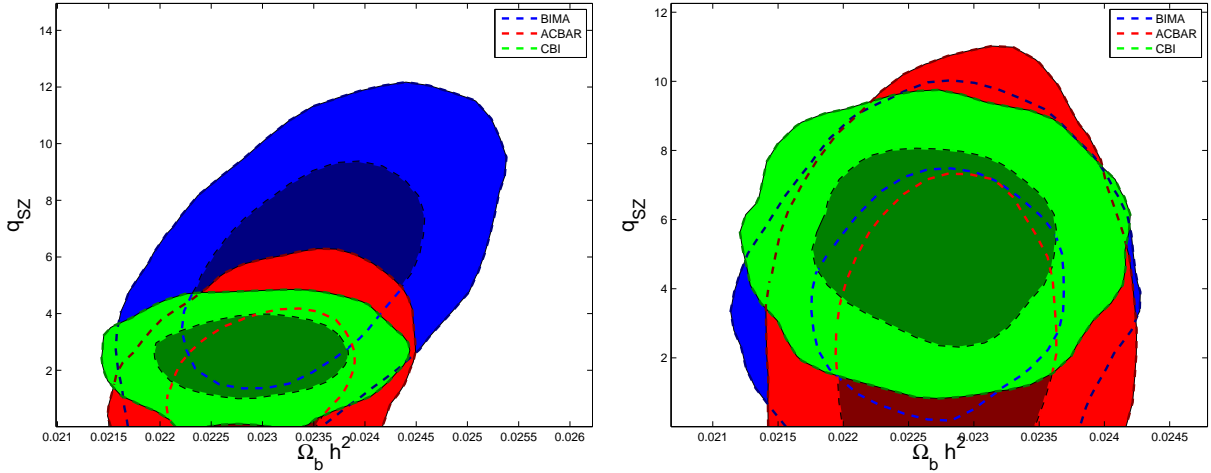


Fig. 7.— 1- and 2- $\sigma$  likelihood contours of the SZ amplitude and the baryon density, as determined from MCMC chains for CBI, ACBAR, and BIMA, as indicated. We ran chains for WMAP5 plus, in turn, CBI, ACBAR, and BIMA, fitting an SZ excess template to each case. The left panel shows the results when using the KSSZ template, and the right panel shows the same using the SPH SZ template, marginalizing over the other parameters. For both templates, the 1- $\sigma$  regions of the three experiments are all in excellent agreement if the excess is due to SZ.

Table 2: CBI Power Spectrum. Power spectrum from the total CBI dataset. Columns are 1) bin, 2) power spectrum, 3) Gaussian error on the power spectrum, 4) thermal noise power in the bin, 5) the contribution from unresolved source in the bin (assuming  $0.046 \text{ Jy}^2/\text{sr}$ ), 6) lower  $\ell$  limit, and 7) upper  $\ell$  limit.

$\ell$	$C_\ell(\mu\text{K}^2)$	Error	$C_{noise}(\mu\text{K}^2)$	$C_{src}(\mu\text{K}^2)$	$\ell_{min}$	$\ell_{max}$
1	5695.372	753.175	1767.465	2.4	0.00	350.00
2	1260.879	260.277	218.186	1.2	350.00	450.00
3	2987.370	408.622	300.134	3.5	450.00	540.00
4	2449.122	376.215	235.321	4.7	540.00	620.00
5	1844.757	268.193	311.309	3.5	620.00	700.00
6	2680.066	346.136	487.124	4.7	700.00	780.00
7	2241.459	312.705	464.681	6.0	780.00	860.00
8	2204.210	313.916	602.316	8.3	860.00	940.00
9	691.900	221.538	600.919	9.9	940.00	1020.00
10	979.649	220.328	555.848	9.5	1020.00	1100.00
11	1166.825	203.100	607.624	11.9	1100.00	1192.00
12	1041.110	166.131	669.178	14.2	1192.00	1302.00
13	727.473	143.316	706.893	13.7	1302.00	1425.00
14	803.088	147.134	1218.974	19.7	1425.00	1600.00
15	311.402	126.647	1240.392	27.4	1600.00	1800.00
16	379.102	122.922	1316.752	29.9	1800.00	2050.00
17	260.743	132.234	1666.893	35.4	2050.00	2350.00
18	386.738	117.427	3000.407	66.1	2350.00	3900.00

Table 3: Cosmological Parameters from CBI+WMAP5. These are the standard basic 6 parameters of the tilted  $\Lambda$ CDM model and the SZ amplitude  $q_{SZ}$ , plus parameters derived from them for CBI and WMAP5. Note that all of the parameters except for  $\sigma_8$ , and the  $\sigma_8$  inferred from the SZ amplitude  $\sigma_8^{SZ} \propto q_{SZ}^{1/7}$  are relatively insensitive to the two SZ templates used. All parameters above the line are independent variables, and those below are derived from the independent parameters.

Parameter	CBI+WMAP5+KS sz	CBI+WMAP5+Bond sz
$\Omega_b h^2$	$0.02291 \pm 0.00061$	$0.02271 \pm 0.00060$
$\Omega_c h^2$	$0.1069 \pm 0.0064$	$0.1081 \pm 0.0063$
$\theta$	$1.0406 \pm 0.0030$	$1.0404 \pm 0.0030$
$\tau$	$0.087 \pm 0.018$	$0.086 \pm 0.018$
$q_{SZ}$	$2.52 \pm 0.96$	$5.3 \pm 1.8$
$n_s$	$0.960 \pm 0.015$	$0.963 \pm 0.015$
$\log[10^{10} A_s]$	$3.039 \pm 0.044$	$3.052 \pm 0.042$
$\Omega_\Lambda$	$0.756 \pm 0.030$	$0.750 \pm 0.030$
$Age/GYr$	$13.65 \pm 0.14$	$13.68 \pm 0.14$
$\Omega_m$	$0.244 \pm 0.030$	$0.250 \pm 0.030$
$\sigma_8$	$0.770 \pm 0.038$	$0.781 \pm 0.036$
$z_{re}$	$10.8 \pm 1.5$	$10.9 \pm 1.5$
$\sigma_8^{SZ}$	$0.910 \pm 0.064$	$1.015 \pm 0.060$
$H_0$	$73.2 \pm 2.8$	$72.6 \pm 2.8$

Table 4: Cosmological Parameters Determined from the Combined CMB Datasets. These are the standard basic 6 parameters of the tilted  $\Lambda$ CDM model and the SZ amplitude  $q_{SZ}$ , plus parameters derived from them for combined CMB datasets (see text for the list). Columns are as in Table 3.

Parameter	WMAP5+CMBall+KS SZ	WMAP5+CMBall+SPH SZ
$\Omega_b h^2$	$0.02289 \pm 0.00057$	$0.02264 \pm 0.00056$
$\Omega_c h^2$	$0.1073 \pm 0.0068$	$0.1088 \pm 0.0054$
$\theta$	$1.0419 \pm 0.0025$	$1.0417 \pm 0.0025$
$\tau$	$0.085 \pm 0.018$	$0.085 \pm 0.017$
$\alpha_{SZ}$	$2.65 \pm 0.81$	$4.3 \pm 1.3$
$n_s$	$0.956 \pm 0.014$	$0.960 \pm 0.014$
$\log[10^{10} A_s]$	$3.033 \pm 0.039$	$3.051 \pm 0.038$
$\Omega_\Lambda$	$0.758 \pm 0.026$	$0.749 \pm 0.027$
$Age/GYr$	$13.62 \pm 0.13$	$13.66 \pm 0.13$
$\Omega_m$	$0.242 \pm 0.026$	$0.251 \pm 0.027$
$\sigma_8$	$0.769 \pm 0.031$	$0.784 \pm 0.030$
$z_{re}$	$10.7 \pm 1.5$	$10.8 \pm 1.5$
$\sigma_8^{SZ}$	$0.922 \pm 0.047$	$0.988 \pm 0.049$
$H_0$	$73.5 \pm 2.6$	$72.6 \pm 2.6$

Table 5: CBI Predictions for Other Experiments. For convenience in comparing the CBI results with other experiments if the excess power is due to SZ, we present the signals predicted by the two SZ templates at a variety of frequencies and angular scales. All values are in  $\mu K^2$ .

$\ell$	30 GHz KS	100 GHz KS	150 GHz KS	30 GHz SPH	100 GHz SPH	150 GHz SPH
500	$48.6 \pm 18.5$	$29.0 \pm 11.0$	$11.6 \pm 4.4$	$24.3 \pm 8.3$	$14.5 \pm 4.9$	$5.8 \pm 2.0$
1000	$73.3 \pm 27.9$	$43.6 \pm 16.6$	$17.4 \pm 6.6$	$52.5 \pm 17.8$	$31.3 \pm 10.6$	$12.5 \pm 4.2$
1500	$87.8 \pm 33.4$	$52.3 \pm 19.9$	$20.9 \pm 8.0$	$94.2 \pm 32.0$	$56.1 \pm 19.1$	$22.4 \pm 7.6$
2000	$94.2 \pm 35.9$	$56.1 \pm 21.4$	$22.4 \pm 8.5$	$138.2 \pm 46.9$	$82.3 \pm 28.0$	$32.9 \pm 11.2$
2500	$96.2 \pm 36.6$	$57.3 \pm 21.8$	$22.9 \pm 8.7$	$151.8 \pm 51.5$	$90.4 \pm 30.7$	$36.1 \pm 12.3$
3000	$96.2 \pm 36.7$	$57.3 \pm 21.8$	$22.9 \pm 8.7$	$189.3 \pm 64.3$	$112.8 \pm 38.3$	$45.0 \pm 15.3$
4000	$92.4 \pm 35.2$	$55.1 \pm 21.0$	$22.0 \pm 8.4$	$232.9 \pm 79.1$	$138.8 \pm 47.1$	$55.4 \pm 18.8$
5000	$86.2 \pm 32.8$	$51.4 \pm 19.6$	$20.5 \pm 7.8$	$280.4 \pm 95.2$	$167.0 \pm 56.7$	$66.7 \pm 22.7$
6000	$80.3 \pm 30.6$	$47.9 \pm 18.2$	$19.1 \pm 7.3$	$294.0 \pm 99.9$	$175.2 \pm 59.5$	$70.0 \pm 23.8$
8000	$67.4 \pm 25.7$	$40.1 \pm 15.3$	$16.0 \pm 6.1$	$316.9 \pm 107.6$	$188.8 \pm 64.1$	$75.4 \pm 25.6$

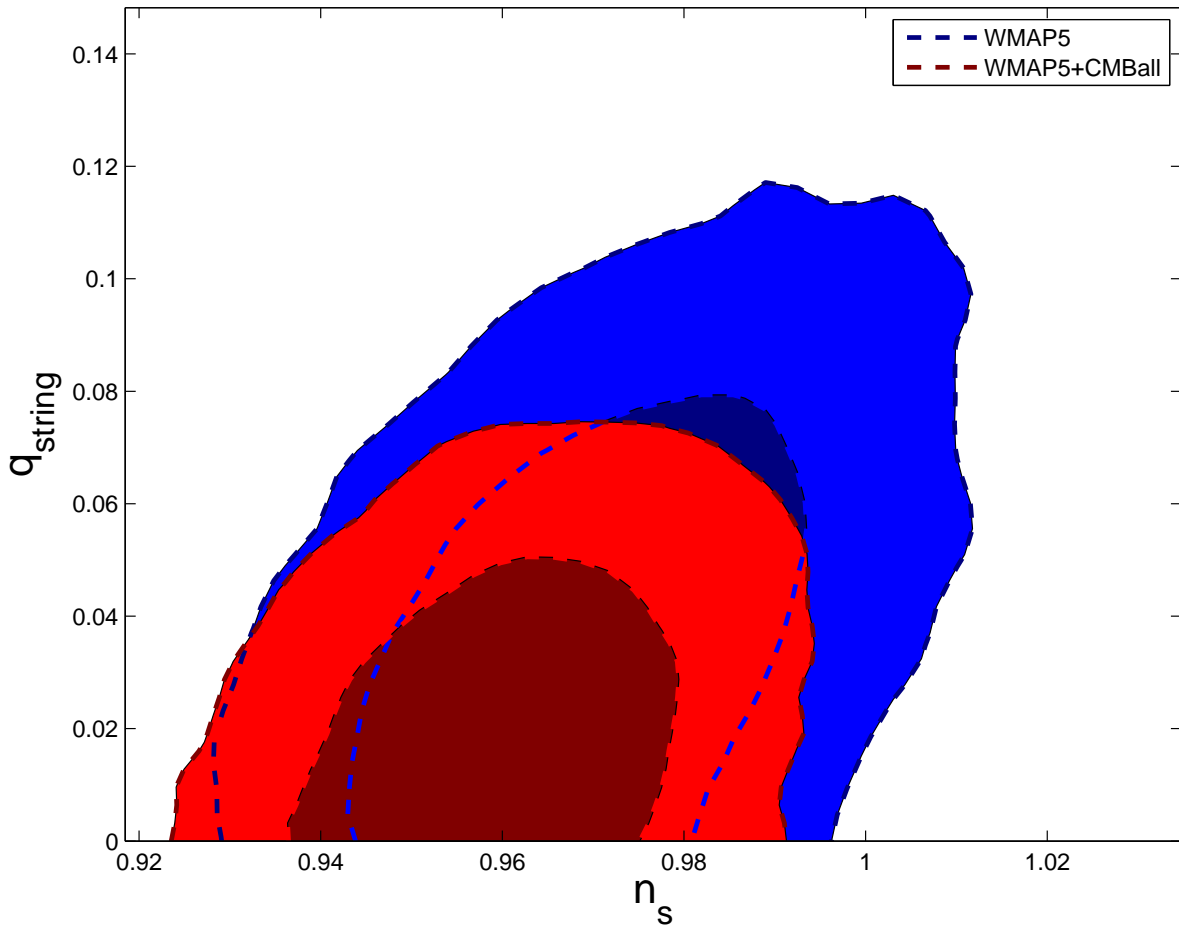


Fig. 8.— 1- and 2- $\sigma$  likelihood contours of cosmic string amplitude and  $n_s$ , marginalized over other parameters. The string amplitude is relative to the  $\mathcal{C}_\ell$ -template of Pogosian et al. (2008), which is normalized to a string tension of  $G\mu = 1.1 \times 10^{-6}$ . With only WMAP5 data,  $n_s$  is partially degenerate with  $q_{string}$ , and  $n_s < 1$  is no longer significant at a 2- $\sigma$  level. The addition of the high- $\ell$  CMB data breaks this degeneracy, and  $n_s < 1$  at the 2- $\sigma$  level holds even with the addition of cosmic strings to the parameter analysis.

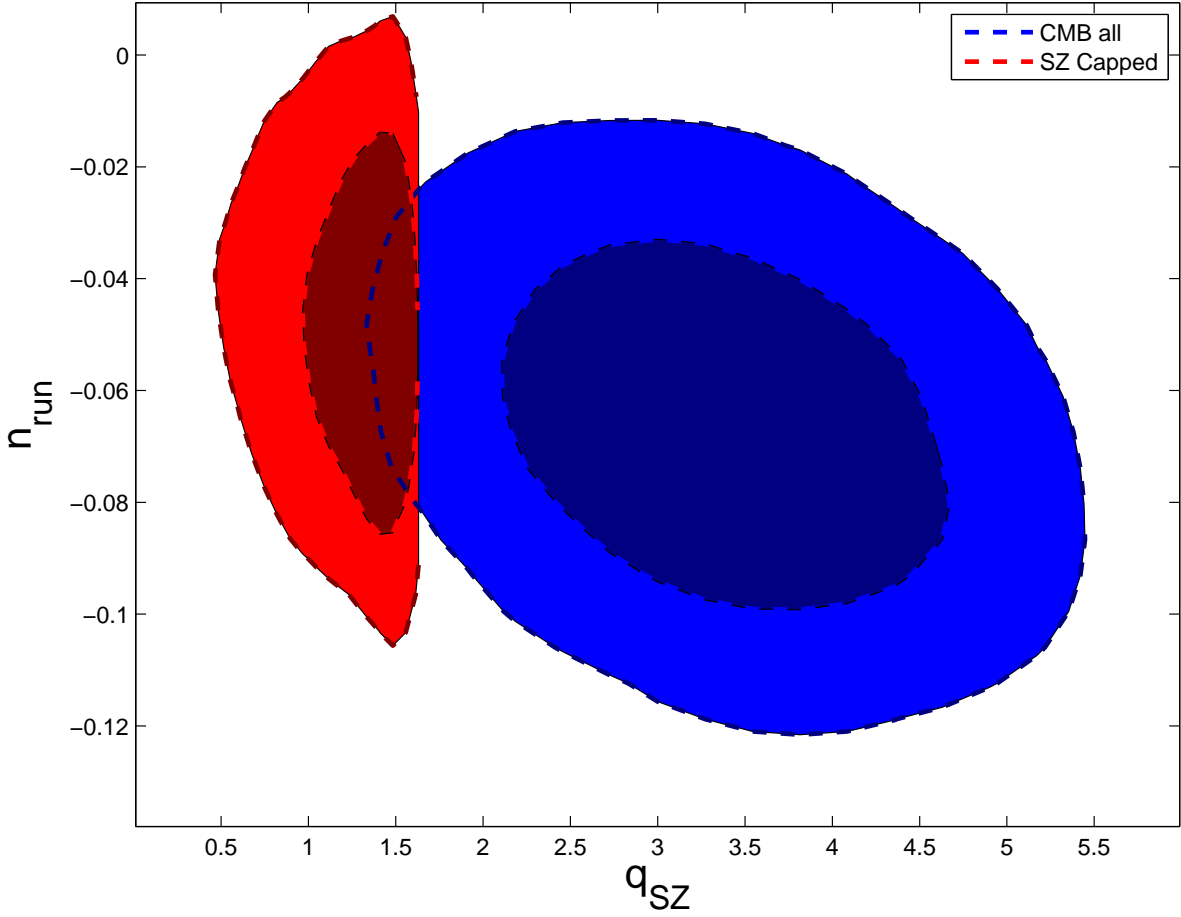


Fig. 9.— 1- and 2- $\sigma$  likelihood contours of the running of the spectral index  $n_{run} = \frac{dn_s}{d\log k}(0.05h \text{ Mpc}^{-1})$ , and SZ amplitude  $q_{SZ}$ , marginalized over other parameters. A high level of the SZ template pulls power out of the primary CMB fluctuations in the region of the third peak. This drives  $\frac{dn_s}{d\log k}$  more negative. The artificial cropping of  $q_{SZ}$  at a value of 2.0 as used in the WMAP5 analysis of Dunkley et al. (2008) clearly distorts the picture relative to a freely floating  $q_{SZ}$ .

- Cleary, K. A., Taylor, A. C., Waldram, E., Battye, R. A., Dickinson, C., Davies, R. D., Davis, R. J., Genova-Santos, R., Grainge, K., Jones, M. E., Kneissl, R., Pooley, G. G., Rebolo, R., Rubiño-Martín, J. A., Saunders, R. D. E., Scott, P. F., Slosar, A., Titterington, D., & Watson, R. A. 2005, *MNRAS*, 360, 340
- Condon, J. J., Cotton, W. D., Greisen, E. W., Yin, Q. F., Perley, R. A., Taylor, G. B., & Broderick, J. J. 1998, *AJ*, 115, 1693
- Davies, R. D., Dickinson, C., Banday, A. J., Jaffe, T. R., Górski, K. M., & Davis, R. J. 2006, *MNRAS*, 370, 1125
- Dawson, K. S., Holzappel, W. L., Carlstrom, J. E., Joy, M., & LaRoque, S. J. 2006, *ApJ*, 647, 13
- de Bernardis, P. et al. 2000, *Nature*, 404, 955
- de Oliveira-Costa, A., Tegmark, M., Davies, R. D., Gutiérrez, C. M., Lasenby, A. N., Rebolo, R., & Watson, R. A. 2004, *ApJ*, 606, L89
- Dickinson, C., Battye, R. A., Carreira, P., Cleary, K., Davies, R. D., Davis, R. J., Genova-Santos, R., Grainge, K., Gutiérrez, C. M., Hafez, Y. A., Hobson, M. P., Jones, M. E., Kneissl, R., Lancaster, K., Lasenby, A., Leahy, J. P., Maisinger, K., Ödman, C., Pooley, G., Rajguru, N., Rebolo, R., Rubiño-Martín, J. A., Saunders, R. D. E., Savage, R. S., Scaife, A., Scott, P. F., Slosar, A., Sosa Molina, P., Taylor, A. C., Titterington, D., Waldram, E., Watson, R. A., & Wilkinson, A. 2004, *MNRAS*, 353, 732
- Dickinson, C., Davies, R. D., & Davis, R. J. 2003, *MNRAS*, 341, 369
- Dobler, G. & Finkbeiner, D. P. 2008a, *ApJ*, 680, 1222
- . 2008b, *ApJ*, 680, 1235
- Draine, B. T. & Lazarian, A. 1998a, *ApJ*, 494, L19+
- . 1998b, *ApJ*, 508, 157
- Dunkley, J., Komatsu, E., Nolta, M. R., Spergel, D. N., Larson, D., Hinshaw, G., Page, L., Bennett, C. L., Gold, B., Jarosik, N., Weiland, J. L., Halpern, M., Hill, R. S., Kogut, A., Limon, M., Meyer, S. S., Tucker, G. S., Wollack, E., & Wright, E. L. 2008, *ArXiv e-prints*, 803
- Finkbeiner, D. P. 2003, *ApJS*, 146, 407

- . 2004, *ApJ*, 614, 186
- Freedman, W. L. et al. 2001, *Astrophys. J.*, 553, 47
- Gautier, III, T. N., Boulanger, F., Perault, M., & Puget, J. L. 1992, *AJ*, 103, 1313
- Halverson, N. W. et al. 2002, *Astrophys. J.*, 568, 38
- Hanany, S. et al. 2000, *Astrophys. J.*, 545, L5
- Hildebrandt, S. R., Rebolo, R., Rubiño-Martín, J. A., Watson, R. A., Gutiérrez, C. M., Hoyland, R. J., & Battistelli, E. S. 2007, *ArXiv e-prints*, 706
- Hill, R. S., Weiland, J. L., Odegard, N., Wollack, E., Hinshaw, G., Larson, D., Bennett, C. L., Halpern, M., Page, L., Dunkley, J., Gold, B., Jarosik, N., Kogut, A., Limon, M., Nolte, M. R., Spergel, D. N., Tucker, G. S., & Wright, E. L. 2008, *ArXiv e-prints*, 803
- Hopkins, A. M., Afonso, J., Chan, B., Cram, L. E., Georgakakis, A., & Mobasher, B. 2003, *AJ*, 125, 465
- Jones, W. et al. 2006, *ApJ*, 647, 823
- Komatsu, E. & Seljak, U. 2002, *MNRAS*, 336, 1256
- Kovac, J. et al. 2002, *Nature*, 420, 772
- Kuo, C. L., Ade, P. A. R., Bock, J. J., Bond, J. R., Contaldi, C. R., Daub, M. D., Goldstein, J. H., Holzzapfel, W. L., Lange, A. E., Lueker, M., Newcomb, M., Peterson, J. B., Reichardt, C., Ruhl, J., Runyan, M. C., & Staniszewski, Z. 2007, *ApJ*, 664, 687
- Kuo, C. L. et al. 2004, *Astrophys. J.*, 600, 32
- Leitch, E. M., Readhead, A. C. S., Pearson, T. J., & Myers, S. T. 1997, *ApJ*, 486, L23+
- Leitch, E. M. et al. 2004, *Astrophys. J.*, 624, L10
- Lewis, A. & Bridle, S. 2002, *Phys. Rev.*, D66, 103511
- Lewis, A., Challinor, A., & Lasenby, A. 2000, *Astrophys. J.*, 538, 473
- Mason, B. S. et al. 2003, *Astrophys. J.*, 591, 540
- . 2008, *Astrophys. J.*, in prep.

- Montroy, T. et al. 2006, *ApJ*, 647, 813
- Myers, S. T. et al. 2003, *Astrophys. J.*, 591, 575
- Nolta, M. R., Dunkley, J., Hill, R. S., Hinshaw, G., Komatsu, E., Larson, D., Page, L., Spergel, D. N., Bennett, C. L., Gold, B., Jarosik, N., Odegard, N., Weiland, J. L., Wollack, E., Halpern, M., Kogut, A., Limon, M., Meyer, S. S., Tucker, G. S., & Wright, E. L. 2008, *ArXiv e-prints*, 803
- Padin, S., Cartwright, J. K., Mason, B. S., Pearson, T. J., Readhead, A. C. S., Shepherd, M. C., Sievers, J., Udomprasert, P. S., Holzapfel, W. L., Myers, S. T., Carlstrom, J. E., Leitch, E. M., Joy, M., Bronfman, L., & May, J. 2001, *ApJL*, 549, L1
- Padin, S. et al. 2002, *Pub. Ast. Soc. Pac.*, 114, 83
- Pearson, T. J. et al. 2003, *Astrophys. J.*, 591, 556
- Perlmutter, S. et al. 1999, *Astrophys. J.*, 517, 565
- Pogosian, L., Tye, S. . H., Wasserman, I., & Wyman, M. 2008, *ArXiv e-prints*, 804
- Press, W., Teukolsky, S., Vetterling, W., & Flannery, B. 1992, *Numerical Recipes in C, Second Edition* (Cambridge University Press)
- Pryke, C. et al. 2008, *ArXiv e-prints*
- Readhead, A. C. S. et al. 2004a, *Astrophys. J.*, 609, 498
- . 2004b, *Science*, 306, 836
- Reichardt, C. L., Ade, P. A. R., Bock, J. J., Bond, J. R., Brevik, J. A., Contaldi, C. R., Daub, M. D., Dempsey, J. T., Goldstein, J. H., Holzapfel, W. L., Kuo, C. L., Lange, A. E., Lueker, M., Newcomb, M., Peterson, J. B., Ruhl, J., Runyan, M. C., & Staniszewski, Z. 2008, *ArXiv e-prints*, 801
- Richards, E. A. 2000, *ApJ*, 533, 611
- Riess, A. et al. 1998, *AJ*, 116, 1009
- Schlegel, D. J., Finkbeiner, D. P., & Davis, M. 1998, *ApJ*, 500, 525
- Schulz, A. E. & White, M. 2003, *ApJ*, 586, 723
- Sievers, J. 2003, PhD thesis, California Institute of Technology

Sievers, J. L., Achermann, C., Bond, J. R., Bronfman, L., Bustos, R., Contaldi, C. R., Dickinson, C., Ferreira, P. G., Jones, M. E., Lewis, A. M., Mason, B. S., May, J., Myers, S. T., Oyarce, N., Padin, S., Pearson, T. J., Pospieszalski, M., Readhead, A. C. S., Reeves, R., Taylor, A. C., & Torres, S. 2007, *ApJ*, 660, 976

White, M. 2003, *ApJ*, 597, 650

White, M., Carlstrom, J. E., Dragovan, M., & Holzappel, W. L. 1999, *ApJ*, 514, 12

## A. Maximum Likelihood Fitting

We use the program MPILIKELY to measure the maximum-likelihood power spectrum and related quantities from the gridded data and its noise and signal matrices. MPILIKELY is an MPI implementation of the algorithm described in Sievers (2003). We briefly summarize the algorithm here, as well as describe additional features of MPILIKELY.

### A.1. Fast Curvature and Gradient Calculation

The likelihood of correlated Gaussian data is:

$$\log(\mathcal{L}) = -\frac{1}{2}\mathbf{d}^\dagger\mathbf{C}^{-1}\mathbf{d} - \frac{1}{2}\log(|\mathbf{C}|) \quad (\text{A1})$$

where  $\mathbf{d}$  is the data, and  $\mathbf{C} = \langle \mathbf{d}_i \mathbf{d}_j \rangle$  is the covariance matrix( *e.g.*, Bond et al. (1998)). The correlation matrix in general will depend on both the noise and the signal in the data. The maximum-likelihood solution is then the set of parameters on which  $\mathbf{C}$  depends that maximizes the likelihood. It is often the case that  $\mathbf{C}$  depends linearly on its parameters. This is true if we parameterize the CMB power spectrum by bands in  $\ell$ , in which case the theory matrix of Equation 2 takes the form

$$\mathbf{C}_T = \sum q_B \mathbf{C}_B, \quad (\text{A2})$$

in terms of CMB signal matrices  $\mathbf{C}_B$  with associated bandpowers  $q_B$ . The standard technique for maximizing the likelihood is to calculate the gradient and curvature of the log-likelihood

and take a multi-dimensional Newton’s method step, iterating until convergence. The gradient of the log likelihood when the theory covariance is of the form given in Equation A2 is:

$$\frac{\partial \log(\mathcal{L})}{\partial q_B} = \frac{1}{2} \mathbf{d}^\dagger \mathbf{C}^{-1} \mathbf{C}_B \mathbf{C}^{-1} \mathbf{d} - \frac{1}{2} \text{Tr}(\mathbf{C}^{-1} \mathbf{C}_B) \quad (\text{A3})$$

where  $\text{Tr}$  is the trace operator. The curvature is:

$$\frac{\partial^2 \log \mathcal{L}}{\partial q_B \partial q'_B} = -\mathbf{d}^\dagger \mathbf{C}^{-1} \mathbf{C}_B \mathbf{C}^{-1} \mathbf{C}_{B'} \mathbf{C}^{-1} \mathbf{d} + \frac{1}{2} \text{Tr}(\mathbf{C}^{-1} \mathbf{C}_B \mathbf{C}^{-1} \mathbf{C}_{B'}) \quad (\text{A4})$$

. It is straightforward to show that

$$\mathbf{a}^\dagger \mathbf{B} \mathbf{a} = \text{Tr}(\mathbf{B} \mathbf{a} \mathbf{a}^\dagger) \quad (\text{A5})$$

for vector  $\mathbf{a}$  and matrix  $\mathbf{B}$ . One can use that identity to rewrite the first term in the curvature as follows:

$$\text{Tr}[\mathbf{C}^{-1} \mathbf{C}_B \mathbf{C}^{-1} \mathbf{C}_{B'} \mathbf{C}^{-1} \mathbf{d} \mathbf{d}^T] . \quad (\text{A6})$$

If the correlation matrix is a good description of the data, we have  $\langle \mathbf{d} \mathbf{d}^T \rangle = \mathbf{C}$ , or equivalently that  $\mathbf{C}^{-1} \mathbf{d} \mathbf{d}^T \simeq \mathbf{I}$ , the identity matrix. At this point, the standard treatment (Bond et al. 2000, *e.g.*,) is to replace  $\mathbf{C}^{-1} \mathbf{d} \mathbf{d}^T$  with  $\mathbf{I}$  which leaves

$$\frac{\partial^2 \log(\mathcal{L})}{\partial q_B \partial q'_B} \simeq -\frac{1}{2} \text{Tr}(\mathbf{C}^{-1} \mathbf{C}_B \mathbf{C}^{-1} \mathbf{C}_{B'}) . \quad (\text{A7})$$

The most efficient implementation when using this approximation requires one to pre-calculate the set matrices  $\mathbf{C}^{-1} \mathbf{C}_B$ , which requires an expensive matrix-matrix multiplication for each bandpower. One can then use the fact that  $\text{Tr}(\mathbf{A} \mathbf{B})$  is an  $n^2$  operation (essentially since one only need calculate the diagonal elements of  $\mathbf{A} \mathbf{B}$ ).

Instead of using  $\langle \mathbf{d} \mathbf{d}^T \rangle \approx \mathbf{C}$  to cancel the first term in the curvature, MPILIKELY uses it to cancel the second term, leaving:

$$\frac{\partial^2 \log(\mathcal{L})}{\partial q_B \partial q'_B} \simeq -\frac{1}{2} \mathbf{d}^T \mathbf{C}^{-1} \mathbf{C}_B \mathbf{C}^{-1} \mathbf{C}_{B'} \mathbf{C}^{-1} \mathbf{d} . \quad (\text{A8})$$

The great advantage of this form of the approximate curvature is that it can be calculated using strictly matrix-vector operations. In practice, on MPI clusters, we find that MPILIKELY typically spends 80-90% of its time inverting the covariance matrix, even when fitting dozens of parameters. In addition, storage requirements are halved since we don’t have to store the set of matrices  $\mathbf{C}^{-1} \mathbf{C}_B$ . We also note that the error in Equation A7 is exactly twice that of A8. However, since the curvature only affects the path taken to the maximum likelihood

solution, both approximations will result in the same bandpowers. For final data products, we typically evaluate the full curvature at convergence for more accurate error bars.

When finding the maximum-likelihood spectrum, MPILIKELY uses a modified version of the Levenberg-Marquardt algorithm (see *e.g.*, Press et al. (1992)) that generally reduces to Newton-Raphson iteration. The Levenberg-Marquardt control parameter  $\lambda$  is initially set to zero, and remains there as long as the covariance remains positive-definite. On the first failure, it is set to unity, under the theory that if the current guess has overshoot the maximum enough to make  $\mathbf{C}$  non-positive-definite, a correction of the step by of order at least a factor of two is warranted. On continued failures, we increase  $\lambda$  by a factor of 2, and on successes, we decrease it by  $\sqrt{2}$  until  $\lambda$  falls below one, at which point we set it to zero. Our convergence criteria are that the largest step in any dimension, in terms of the error in that dimension, is less than some small fraction ( typically 0.01), and that  $\lambda = 0$  during that iteration. In practice,  $\lambda$  stays at zero, unless there is a power spectrum bin that is significantly negative. This happens when a random realization of the noise has substantially less power in it than expected, which pushes the power spectrum negative and introduces substantial skewness to the likelihood.

## A.2. Spectrum From Matrices

It is useful to be able to calculate the power spectrum and errors expected from either a noiseless data vector or a signal matrix. The treatment for the two cases is similar. We can invoke the identity in Equation A5, replace  $\mathbf{d}\mathbf{d}^T$  with the matrix  $\mathbf{D}$ , and take advantage of the fact that  $Tr(\mathbf{A}\mathbf{B}) = Tr(\mathbf{B}\mathbf{A})$  to rewrite the gradient as follows:

$$\frac{\partial \log(\mathcal{L})}{\partial q_B} = \frac{1}{2} Tr(\mathbf{C}^{-1}\mathbf{D}\mathbf{C}^{-1}\mathbf{C}_B) - \frac{1}{2} Tr(\mathbf{C}^{-1}\mathbf{C}_B). \quad (\text{A9})$$

We can now find the expected spectrum from data drawn from covariance matrix  $\mathbf{D}$ , marginalized over realizations of the data. When fitting to noiseless data, we have  $\mathbf{D} = \mathbf{d}\mathbf{d}^T + \mathbf{C}^N$  to marginalize over realizations of the noise. The gradient calculation is slowed by a factor of  $\sim 3$  since we now have to calculate  $\mathbf{C}^{-1}\mathbf{D}\mathbf{C}^{-1}$  instead of just  $\mathbf{C}^{-1}$ . The curvature calculation is slightly more complicated. Without an actual data vector, we cannot take advantage of the fast curvature calculation in Equation A8. While one could use the curvature in Equation A7, this can become prohibitively slow in practice. MPILIKELY’s solution is to draw a set of sample data vectors from  $\mathbf{D}$ , and then average Equation A8 for each of those realizations. The only  $n^3$  operation this requires is a single initial Cholesky factorization of  $\mathbf{D}$  to calculate the data vectors.

### A.3. Source Projection

The standard way of removing point sources with known positions is by projecting them from the covariance matrix (Bond et al. 2000; Mason et al. 2003, *e.g.*, ). This is roughly equivalent to masking out the source location in the map. In practice, this is done by adding  $\mathbf{C}^{src} = \beta s_i s_i^\dagger$  to the covariance matrix, where  $s_i$  is the signal expected from the  $i^{th}$  source, and  $\beta$  is an (extremely large) amplitude. For sufficiently large  $\beta$ , the power spectrum is insensitive to any signal proportional to  $s_i$  - *i.e.*, we don't need to know the amplitude of the source. We have previously used large values of  $\beta$ , the projection amplitude, but this can lead to numerical stability problems as large  $\beta$ 's cause  $\mathbf{C}$  to become ill-conditioned. Instead, in MPILIKELY we take the analytic limit as  $\beta \rightarrow \infty$  using the Woodbury formula (Press et al. 1992, see *e.g.*, ). For symmetric matrices, we have

$$\lim_{\beta \rightarrow \infty} (\mathbf{C} + \beta \mathbf{S} \mathbf{S}^\dagger)^{-1} = \mathbf{C}^{-1} - \mathbf{C}^{-1} \mathbf{S} (\mathbf{S}^\dagger \mathbf{C}^{-1} \mathbf{S})^{-1} \mathbf{S}^\dagger \mathbf{C}^{-1}. \quad (\text{A10})$$

One must also guard against the possibility of  $\mathbf{S}$  being degenerate. If it is, the calculation of  $(\mathbf{S}^\dagger \mathbf{C}^{-1} \mathbf{S})^{-1}$  will fail. To deal with this possibility, we first scan  $\mathbf{S}$  for repeated columns (same source entered twice). We then orthogonalize  $\mathbf{S}$  through use of a QR factorization, and use the orthogonal matrix  $\mathbf{Q}$  in Equation A10 instead of  $\mathbf{S}$ . One could also use SVD, but QR is typically a factor of  $\sim 6$  faster. With the addition of the QR factorization, the Woodbury formula never requires the inversion of an ill-conditioned matrix, and so as long as the source-free version of the covariance  $\mathbf{C}$  is well-conditioned, source projection does not lead to numerical instability in calculating the source-projected  $\mathbf{C}^{-1}$ .

### A.4. Likelihood Evaluations

It is often useful to directly evaluate the likelihood of a given covariance matrix. Some instances where this is useful are when comparing the goodness-of-fit of two different models for the data, or when measuring quantities like confidence intervals that depend on the non-Gaussian nature of the likelihood surface. The analytic projection of sources using the Woodbury formula complicates likelihood evaluations because  $\mathbf{C}^{-1}$  becomes singular (the projected modes are truly gone). The solution is to rotate into the subspace spanned by the complement of the source vectors. The rotation/compression matrix can also be found efficiently through a QR factorization of the source vectors (most QR implementations also have a way to find an orthogonalized matrix spanning the complement of the original matrix). Each matrix (noise, banded signal...) and the data are then compressed. One could fit the spectrum with these compressed matrices, which gives the same spectrum one gets when using Equation A10. Since the matrices are smaller, the actual fitting of the power spectrum

is sped up. However, the initial overhead required (2 matrix-matrix multiplications for each CMB band, plus typically a few others) is generally much larger than the total time to fit the spectrum with the uncompressed matrices, and so we in general only compress the matrices if we desire likelihoods.

### A.5. Template Fitting

MPILIKELY also supports simultaneous fitting of additive templates to the data when measuring the power spectrum. We use this for measuring the amplitude of foreground maps in the CBI data. For additive templates, the template model is subtracted from the data before calculating the likelihood, which then becomes:

$$\log(\mathcal{L}) = -\frac{1}{2}\mathbf{d}^{*\dagger}\mathbf{C}^{-1}\mathbf{d}^* - \frac{1}{2}\log(|\mathbf{C}|) \quad (\text{A11})$$

where  $\mathbf{d}^* = \mathbf{d} - \sum a_j \mathbf{m}^j$  for expected signal  $\mathbf{m}^j$  with amplitude  $a_j$  and observed data  $\mathbf{d}$ . Here, the index  $j$  runs over templates, not over data elements. The gradient and curvature of the CMB terms are unchanged, as long as they are calculated using  $\mathbf{d}^*$  instead of  $\mathbf{d}$ . The template terms in the gradient are:

$$\frac{\partial \log(\mathcal{L})}{\partial a_j} = \mathbf{m}^{j\dagger} \mathbf{C}^{-1} \mathbf{d}^*. \quad (\text{A12})$$

The curvature terms are:

$$\frac{\partial^2 \log(\mathcal{L})}{\partial a_j \partial a_{j'}} = -\mathbf{m}^{j\dagger} \mathbf{C}^{-1} \mathbf{m}^{j'} \quad (\text{A13})$$

and

$$\frac{\partial^2 \log(\mathcal{L})}{\partial a_j \partial q_B} = -\mathbf{m}^{j\dagger} \mathbf{C}^{-1} \mathbf{C}_B \mathbf{C}^{-1} \mathbf{d}. \quad (\text{A14})$$

These curvature and gradient terms only require matrix-vector operations to calculate, and so have a negligible impact on the time required to fit the power spectrum.